CANCER

Select EZH2 inhibitors enhance viral mimicry effects of DNMT inhibition through a mechanism involving NFAT:AP-1 signaling

Alison A. Chomiak[1]†, Rochelle L. Tiedemann[1]†, Yanqing Liu[1], Xiangqian Kong[2]‡, Ying Cui[2], Ashley K. Wiseman[1], Kate E. Thurlow[1], Evan M. Cornett[3], Michael J. Topper[2], Stephen B. Baylin[2], Scott B. Rothbart[1]*

DNA methyltransferase inhibitor (DNMTi) efficacy in solid tumors is limited. Colon cancer cells exposed to DNMTi accumulate lysine-27 trimethylation on histone H3 (H3K27me3). We propose this Enhancer of Zeste Homolog 2 (EZH2)–dependent repressive modification limits DNMTi efficacy. Here, we show that low-dose DNMTi treatment sensitizes colon cancer cells to select EZH2 inhibitors (EZH2is). Integrative epigenomic analysis reveals that DNMTi-induced H3K27me3 accumulates at genomic regions poised with EZH2. Notably, combined EZH2i and DNMTi alters the epigenomic landscape to transcriptionally up-regulate the calcium-induced nuclear factor of activated T cells (NFAT):activating protein 1 (AP-1) signaling pathway. Blocking this pathway limits transcriptional activating effects of these drugs, including transposable element and innate immune response gene expression involved in viral defense. Analysis of primary human colon cancer specimens reveals positive correlations between DNMTi-, innate immune response–, and calcium signaling–associated transcription profiles. Collectively, we show that compensatory EZH2 activity limits DNMTi efficacy in colon cancer and link NFAT:AP-1 signaling to epigenetic therapy–induced viral mimicry.

INTRODUCTION

Abnormal DNA methylation patterning and its associations with altered gene expression are an enabling hallmark of nearly all human cancers (*1*). This presents as global DNA hypomethylation coupled with focal DNA hypermethylation at CpG-rich promoters [i.e., CpG islands (CGIs)] that contributes to tumor suppressor gene (TSG) silencing (*2*–*5*). Hence, DNA methyltransferase inhibitors (DNMTis), including the nucleoside analogs 5-azacytidine (AZA) and 5-aza-2′-deoxycytidine (DAC; decitabine) are clinically applied as epigenetic therapies with the goal of reversing focal DNA methylation–mediated transcriptional silencing. DNMTis also activate a "viral mimicry" response triggered by derepression of endogenous retroviruses and other transposable elements (TEs) that stimulate double-stranded RNA (dsRNA)–and double-stranded DNA (dsDNA)–dependent expression of innate immune signaling pathways (*6*–*8*). These data suggest that DNMT inhibition might enhance the efficacy of immune checkpoint therapy, as has been demonstrated in preclinical models (*9*–*11*).

Colorectal cancer (CRC) is a leading cause of global cancer deaths (*12*) and has been well characterized for its abnormal DNA methylation patterns (*13*), yet therapeutic treatment with DNMTis in this and other solid tumor contexts has been limited (*14*–*16*). These drugs have short half-lives, and their activity depends on DNA replication. Moreover, high doses of DNMTis cause DNA damage and cytotoxicity (*17*, *18*) and, therefore, are unlikely to improve treatment efficacy in solid tumors. In contrast, repeated exposure to low-dose DNMTis generates stronger and more sustained epigenetic effects (*17*, *19*–*23*). However, the potential benefits of low-dose DNMTi therapy for solid tumors has not materialized in clinical trials (*15*, *16*, *24*).

EZH2, the histone methyltransferase subunit of Polycomb repressive complex 2 (PRC2), catalyzes all three states of lysine-27 methylation on histone H3 (H3K27me) (*25*). PRC2 activity is essential in cell differentiation and development, where H3K27me3, a histone posttranslational modification (PTM) associated with facultative heterochromatin and transcriptional repression, co-occurs at select promoters with H3K4me3, a histone PTM associated with active transcription (*26*, *27*). This "bivalent" or "poised" chromatin state is most commonly found at unmethylated CGI promoters of repressed lineage commitment genes in stem cells, enabling rapid gene activation or continued repression depending on the cellular differentiation cues (*26*). In cancer, these developmentally important bivalent genes are instead stably silenced through focal DNA hypermethylation (*28*–*32*). Targeting this pathologic DNA hypermethylation through genetic or chemical disruption of DNMTs results in a reemergence of the stem-like chromatin state associated with PRC2 activity that reinforces pathologic transcriptional silencing (*28*, *30*, *31*, *33*).

We hypothesize that compensatory silencing through H3K27me3 may explain the barrier to robust and complete clinical responses to DNMTi therapy in solid tumors. This hypothesis is supported by recent studies showing that DNA hypomethylation, induced genetically or as a consequence of chemotherapeutic and metabolic perturbation, sensitizes cancer cells to EZH2 inhibition (*34*–*36*). Moreover, antineoplastic/therapeutic effects have also been shown for multiple cancer cell lines and tumor xenografts treated with DNMT and EZH2 inhibitors (EZH2is) (*10*, *37*–*40*). However, most

---

[1] Department of Epigenetics, Van Andel Institute, Grand Rapids, MI 49503, USA. [2] Department of Oncology, the Sidney Kimmel Comprehensive Cancer Center at Johns Hopkins, The Johns Hopkins University School of Medicine, Baltimore, MD 21287, USA. [3] Department of Biochemistry and Molecular Biology, Indiana University School of Medicine, Indiana University, Indianapolis, IN 46202, USA.
*Corresponding author. Email: scott.rothbart@vai.org
†These authors contributed equally to this work.
‡Present address: State Key Laboratory of Respiratory Disease, Guangzhou Institutes of Biomedicine and Health, Chinese Academy of Sciences, Guangzhou 510530, China.

clinical applications of EZH2is have focused on cancers addicted to PRC2 activity resulting from activating mutations in EZH2 or loss-of-function mutations in the SWItch/Sucrose Non-Fermentable (SWI/SNF) chromatin remodeling complex (*41*–*43*). Thus, combining EZH2is with DNMTis presents an opportunity to expand the utility of these epigenetic agents for cancer therapy.

In this study, we sought to dissect the relationship between DNA methylation and PRC2 activity as repressive transcriptional regulatory mechanisms in CRC and to evaluate the molecular effects of blocking these two nodes of epigenetic signaling as a potential cancer management strategy. We show that CRC cells that are insensitive to single-agent EZH2 inhibition become sensitive as compensatory H3K27me3-mediated silencing emerges upon DNMTi treatment. Epigenomic and transcriptomic analyses indicate that the calcium–calcineurin–nuclear factor of activated T cells (NFAT) signaling pathway is at the nexus of where an epigenetic shift coincides with a transcriptional response. These insights into epigenetic cross-talk suggest a rational drug combination that could enhance the use of DNMTi therapies in solid tumors, while also directing EZH2is in previously unexplored clinical directions.

RESULTS

Select EZH2is synergize with DNMTis to reactivate an epigenetically silenced TSG

Although H3K27me3 accumulation following DNMTi treatment has been reported, the molecular mechanism and consequences of this epigenetic plasticity are unclear. We first considered whether targeting EZH2 augments the transcriptional activating effects of DAC by measuring endogenous *SFRP1* expression in an engineered colon cancer cell line. *SFRP1* is a TSG that is epigenetically silenced by promoter CGI hypermethylation in colon cancer and acquires EZH2-dependent H3K27me3 following DNA hypomethylation (fig. S1A) (*33*, *44*). We inserted a NanoLuciferase (NLuc) cassette into exon 2 of the endogenous *SFRP1* locus of HCT116 cells (Fig. 1A). An EZH2-dependent global increase in H3K27me3 following DAC treatment was also observed in this cell line (fig. S1B), while treatment with either DAC or an EZH2i did not change expression of PRC2 subunits or DNA methylation–associated machinery (fig. S1C). Of note, this reporter cell line was engineered in an HCT116 DNMT1 hypomorphic (MT1) cell line characterized by ~20% reduction in global DNA methylation to enhance the sensitivity to DNA hypomethylating agents (*45*). NLuc activity (a proxy for *SFRP1* expression) was readily detected following DNMT1 knockdown and in a DAC dose- and time-dependent manner coinciding with dose-dependent loss of DNA methylation in the promoter CGI (Fig. 1B and fig. S1D).

The appreciation that certain cancer types are driven by PRC2 hyperactivity has resulted in the development of numerous EZH2is that are routinely used in the laboratory setting and in clinical trials (*46*, *47*). We screened a panel of the most common of these *S*-adenosyl-L-methionine (SAM)–competitive small-molecule EZH2is (fig. S1E) (*47*, *48*) for their ability to reactivate *SFRP1*. With an acute 72-hour treatment, tazemetostat (TAZ or EPZ6438), CPI-1205, and EPZ011989 (a derivative of TAZ) induced *SFRP1* expression and subsequent NLuc reporter activity over a broad range of concentrations, whereas other EZH2is induced only marginal *SFRP1* reactivation (Fig. 1C and fig. S1F). When we combined these EZH2is with a fixed low dose of DAC (30 nM) that had limited single-agent activity in the NLuc assay (Fig. 1B), moderate global effects on DNA methylation loss (fig. S1G), and limited effects on DNA damage by proxy of γH2AX staining (*49*, *50*), we observed a 10-fold increase in *SFRP1* reactivation relative to single-agent EZH2i treatment, with TAZ and CPI-1205 again having the strongest synergistic effects. (Fig. 1D and fig. S1F).

As TAZ had the greatest combined effect with DAC and is the most clinically advanced EZH2i, with Food and Drug Administration approvals for epithelioid sarcoma and follicular lymphoma (*42*, *43*), we considered how it might augment the transcriptional activating effects of DNMT inhibition. We combined TAZ at a fixed dose with either DAC or the non-nucleoside DNMT1 inhibitor GSK3484862 over a range of concentrations that induce comparable dose-dependent loss of DNA methylation across the *SFRP1* promoter in wild-type HCT116 (fig. S1H). TAZ amplified DNMTi-induced up-regulation of the *SFRP1* NLuc reporter by more than fivefold (Fig. 1E). Notably, the maximum NLuc reporter assay signal plateaued and remained elevated at high doses of GSK3484862, whereas DAC with or without TAZ showed a bell curve of activity with a maximum NLuc signal at 300 nM (Fig. 1E). This difference could be related to the induction of toxicity by DAC at high doses, which is suggested, by comparison to GSK3484862, to be DNA hypomethylation independent. Pairwise TAZ and DAC dose-response titrations quantified by Bliss synergy scores of 33.00 and 131.984 at 3 and 6 days after treatment, respectively, support a synergistic interaction (as defined by a Bliss score of >10) for these drugs as modulators of *SFRP1* expression across broad dose ranges (Fig. 1F) (*51*). The selective ability for TAZ to synergize with DAC was further confirmed by quantitative reverse transcription polymerase chain reaction (qRT-PCR) of *SFRP1* expression in wild-type and MT1 HCT116 (fig. S1I). Collectively, these data show that select EZH2is synergize with DNMTis to stimulate expression of an epigenetically silenced TSG in colon cancer.

Single-agent EZH2i potency does not correlate with cytotoxicity

We assumed that the superior ability of TAZ and CPI-1205 to reactivate *SFRP1* was related to their enhanced potency as EZH2is. Western blot analysis of HCT116 cell lysates showed that both TAZ and CPI-1205 dose-dependently reduced global levels of H3K27me3 and did so at lower concentrations than four other EZH2is (Fig. 2A and fig. S2, A and B) despite similar in vitro half maximal inhibitory concentration (IC_{50}) values for PRC2 inhibition (fig. S2C). Unexpectedly, potency was not associated with cellular toxicity. Dose-response cell viability assays showed that MT1 (Fig. 2B) and wild-type HCT116 (fig. S2D) cells tolerated high concentrations of TAZ or CPI-1205 relative to GSK126, GSK503, GSK343, or UNC1999 (Fig. 2B and fig. S2D). These findings of toxicity despite less potent EZH2 inhibition suggest off-target activity separate from their ability to inhibit EZH2. In comparison, that TAZ and CPI-1205 are potent EZH2is with low toxicity is ideal for prolonged treatment regimens where the epigenetic effects of DNMTis require active cell replication and DNA synthesis over a prolonged course of treatment.

Combined DNMT and EZH2 inhibition reduces colon cancer cell proliferation

We next sought to determine whether DNMT inhibition could sensitize colon cancer cells to EZH2 inhibition. We first compared the

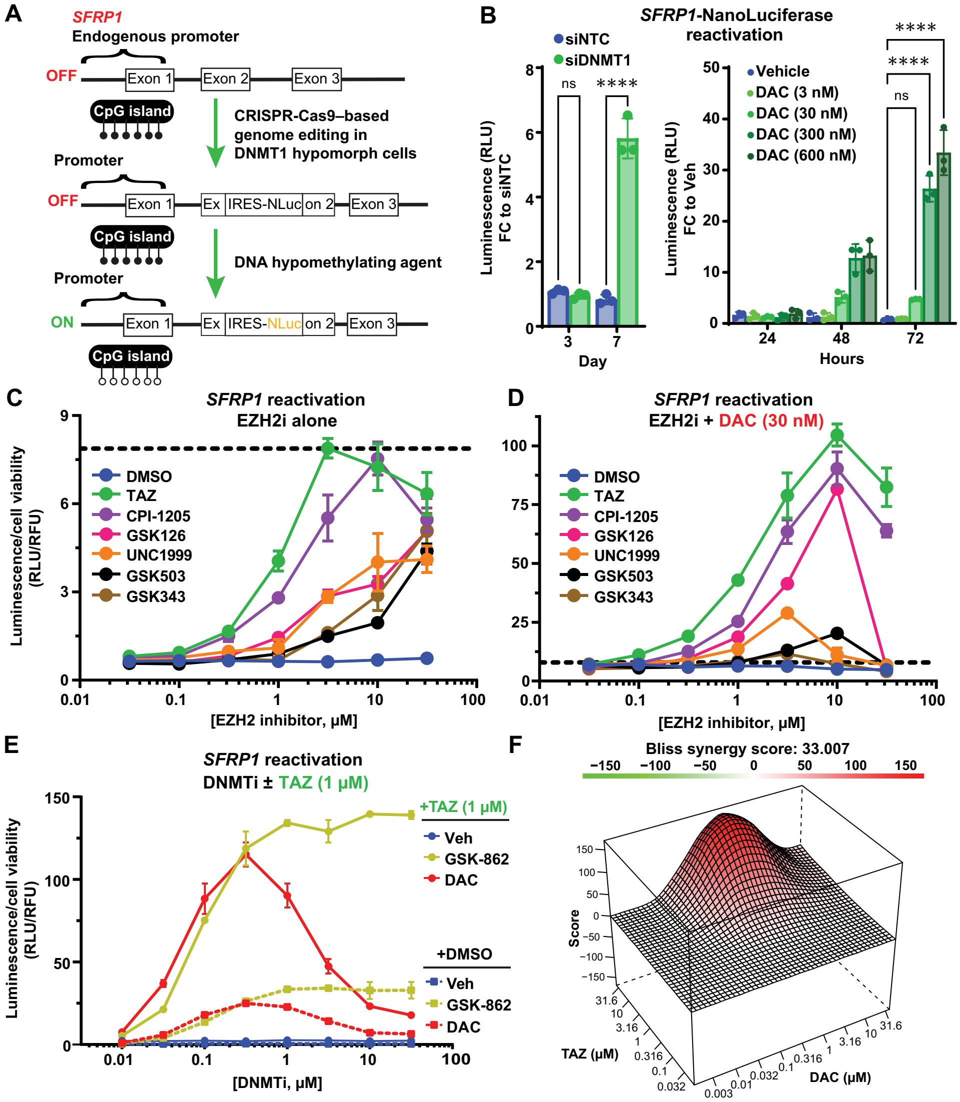

Fig. 1. Select EZH2is enhance the transcriptional activating effects of DNA hypomethylating agents. (**A**) Approach for generating an in-cell endogenous *SFRP1*-NLuc reporter assay in HCT116 cells with hypomorphic DNMT1. IRES, internal ribosomal entry site. (**B**) Reactivation of the silenced *SFRP1* locus small interfering RNA (siRNA)–mediated DNMT1 knockdown (left) or DAC treatment (right). Relative luminescence units (RLU) are shown as fold change (FC) over control at the first time point. siNTC, siRNA nontargeting control; Veh, vehicle. Data are representative of three biological replicates, and the means ± SD of technical triplicates from a single experiment is shown. Statistical significance calculated using two-way analysis of variance (ANOVA) (****$P < 0.0001$). ns, not significant. (**C** and **D**) NLuc reporter activity measurements following 72-hour treatment with the indicated EZH2is alone (C) or in combination (D) with a fixed concentration of DAC. RLU are normalized to relative fluorescence units (RFU) from CellTiter-Fluor cell viability assay to account for cell number. Data are representative of three biological replicates, and the means ± SD of technical triplicates from a single experiment is shown. Dashed black lines denote scaling difference between (C) and (D). (**E**) NLuc reporter activity measurements following 72-hour treatment with the DNMTis DAC or GSK3484862 alone (dashed lines) or in combination with a fixed concentration of TAZ (solid lines). RLU are normalized to RFU from CellTiter-Fluor cell viability assay. Data are representative of three biological replicates, and the means ± SD of technical triplicates from a single experiment is shown. (**F**) Surface plot and Bliss synergy score of DAC + TAZ dose-response curves derived from the *SFRP1*-NLuc reporter assay after 72-hour treatment. Data presented are representative results of two biological replicates. See also fig. S1.

potent but nontoxic TAZ to a less potent but more toxic EZH2i (GSK343) in combination with DAC. When exposed to drugs for 7 days, DAC plus TAZ showed combined efficacy at reducing cell viability (fig. S3A). Conversely, the strong single-agent toxicity of GSK343 reduced cell viability to such an extent, both acutely (3 days) and over time (7 days), that it prevented any therapeutic cooperation with DAC (fig. S3A).

We extended this observation of an acute combination effect on cell viability in HCT116 to monitoring confluency as a measure of outgrowth over time following exposure to DAC, TAZ, or the combination across five colon cancer cell lines representative of the major genetic and epigenetic subtypes of this disease (*52*). Consistent with prior results (Fig. 2B and fig. S3A), single-agent TAZ showed limited antiproliferative effects (Fig. 3A), even at doses sufficient to

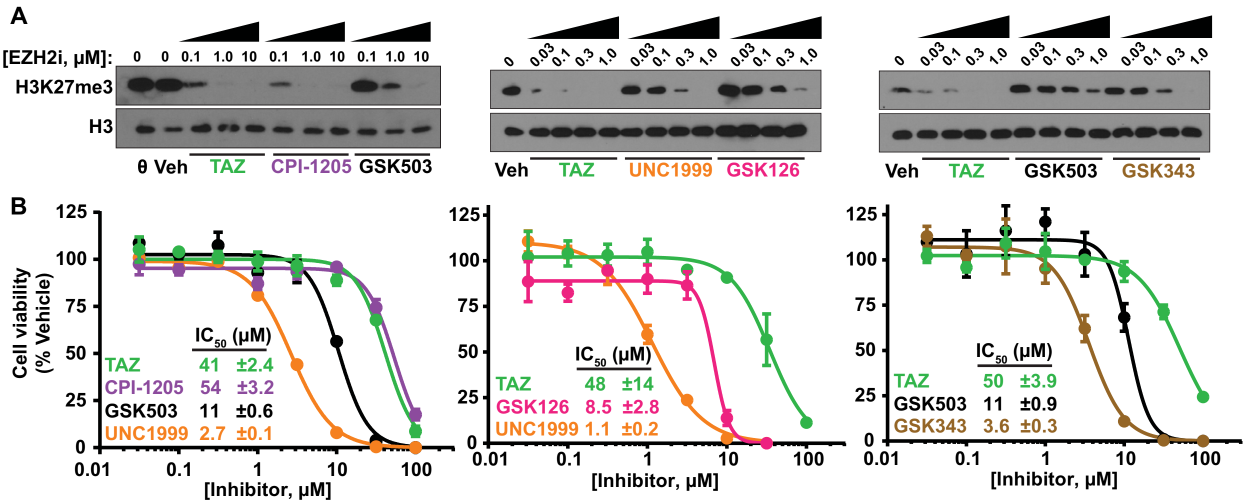

Fig. 2. Single-agent EZH2i potency and therapeutic efficacy do not correlate in HCT116. (**A**) Western blot analysis of H3K27me3 from wild-type HCT116 cells following 72-hour exposure to vehicle (DMSO, % equivalent) or EZH2is at the indicated concentrations. (**B**) Dose-response viability curves (CellTiter-Fluor normalized to vehicle) for *SFRP1*-NLuc reporter/DNMT1 hypomorph HCT116 cells exposed to the indicated EZH2is for 72 hours. Data are representative of three biological replicates, and the means ± SD of technical triplicates from a single experiment is shown. See also fig. S2.

induce loss of H3K27me3 in these cell lines (fig. S3B) and that far exceeded the IC_{50} of TAZ for sensitive cell types (*53*–*55*). However, when combined with doses of DAC that showed limited to moderate single-agent toxicity in culture and reflect the degree of DNA methylation loss achieved in clinical trials (fig. S1C) (*14*, *56*), we observed similar inhibition of cell outgrowth across the colon cancer cell line panel. Although these drugs reduced DNA and histone methylation as early as 3 days at these doses (fig. S3, B and C), these combination effects were most pronounced following multiple low-dose treatments over a pretreatment period of up to 9 days, followed by outgrowth (Fig. 3A and fig. S3D). If single-agent exposures were elevated to concentrations beyond the minimum for inducing epigenetic effects at 3 days (fig. S3, B and C), the combined antiproliferative response could be observed after just a single treatment (fig. S3, A and E to G). However, the prolonged treatments at lower doses are more likely to reflect the positive effects observed from low-dose drug exposure over time that maximizes epigenetic effects in laboratory and clinical trial settings (*17*, *20*–*23*, *57*).

Similar results were obtained when treating ex vivo small intestine adenoma–derived tumoroids from $Apc^{Min/+}$ mice (Fig. 3B). While tumoroids treated with single-agent TAZ or DAC showed nominal changes to morphology, tumoroids treated with combined TAZ and DAC were characterized by reduced size and notable alteration to the standard cyst-like, spherical morphology observed in vehicle-treated tumoroids (Fig. 3, B and C, and fig. S3H) (*58*). These results are consistent with growth measurements from ovarian cancer and prostate cancer xenograft studies in mice exposed to combined inhibition of DNMT1 and EZH2 (*10*, *39*). Collectively, these data show that TAZ and DAC have combined therapeutic efficacy in a temporal- and concentration-dependent manner, limiting cell proliferation in multiple colon cancer cell lines and intestinal tumoroid models that are insensitive to single-agent EZH2 inhibition.

DNMT inhibition induces H3K27me3 accumulation at genomic regions poised with EZH2

The combined molecular and therapeutic efficacy of DNMT and EZH2 inhibition suggested that a PRC2 dependency emerges following hypomethylation of the genome. To test this hypothesis, we performed quantitative epigenomic analyses for DNA methylation and H3K27me3 in response to these drug treatments after 72 hours when global changes to these modifications can be observed (Fig. 2A and fig. S1, A and B). Doses chosen for each drug were in the range of synergy identified from Fig. 1. TAZ treatment had no effect on genome-wide DNA methylation patterns, and the combination of TAZ with a low dose of DAC (30 nM; DAC30) did not further deplete DNA methylation relative to DAC treatment alone (figs. S1G and S4, A and B). Drug-induced DNA hypomethylation occurred at the same CpG loci (fig. S4A) and to the same degree for both single-agent DAC and combination treatments (fig. S4B; average $\Delta\beta \cong -0.14$). Last, these conserved DNA hypomethylation events occurred primarily across gene promoters and distal regulatory space defined as at least five contiguous Infinium MethylationEPIC array probes that fell either in intergenic or intronic regions (fig. S4C).

We then used our recently developed sans spike-in quantitative chromatin immunoprecipitation sequencing (ChIP-seq) method (siQ-ChIP) (*59*, *60*) to quantify changes in H3K27me3 after drug treatment (fig. S4, D to G). TAZ treatment alone and in combination with DAC substantially reduced H3K27me3 levels across the genome (Fig. 4, A and B). We next built custom ChromHMM annotations for HCT116 cells to query where H3K27me3 loss primarily occured in the genome after TAZ treatment (fig. S4, H and I). As expected, H3K27me3 loss for single-agent TAZ and combination treatments was most pronounced in Polycomb repressive regions (ReprPC1, ReprPC2, and EnhBiv) that had abundant H3K27me3 signal in vehicle-treated cells (Fig. 4C, left). In addition to ChromHMM annotations, we considered new genomic studies that place H3K27me3 at crucial transition regions of the genome. H3K27me3

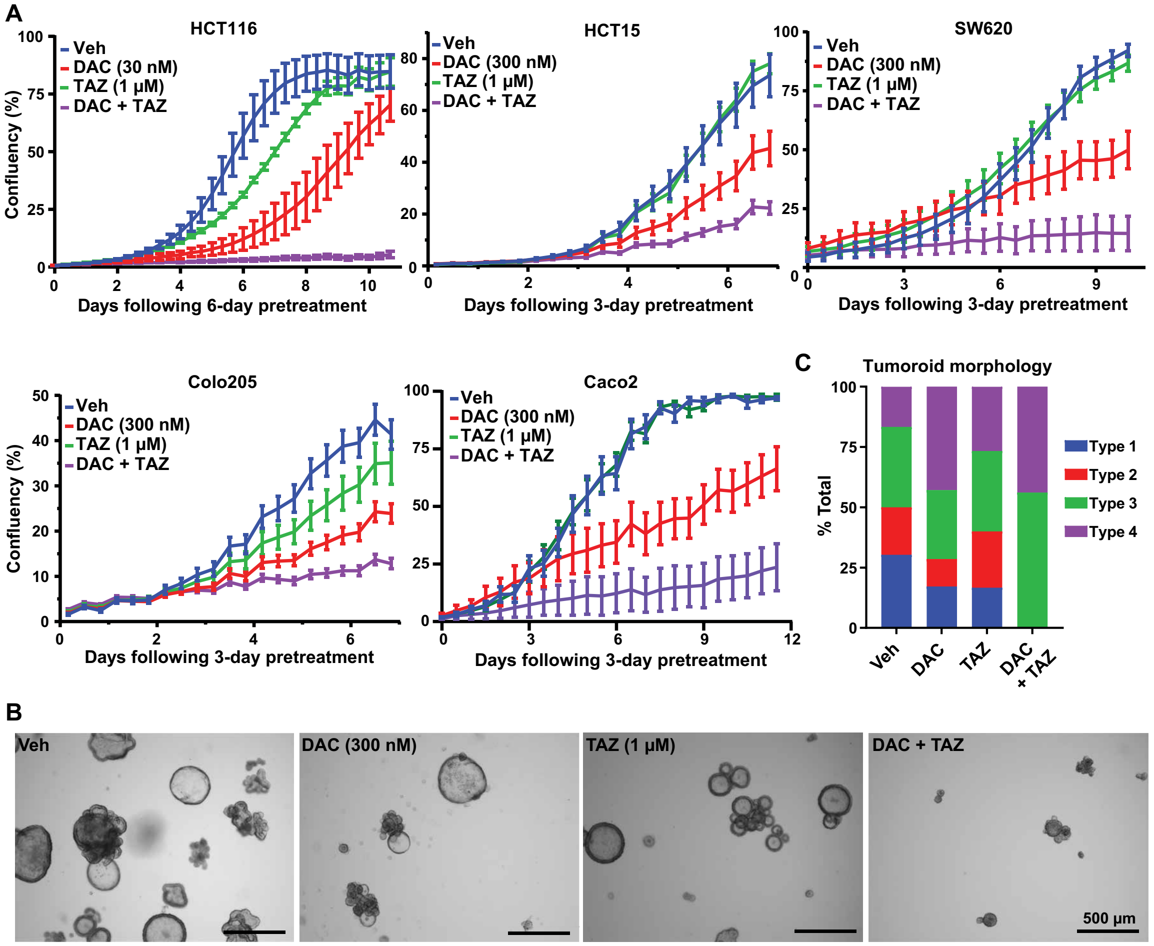

Fig. 3. DAC and TAZ synergize to reduce colon cancer cell and tumoroid proliferation. (**A**) Confluency measurements of the indicated colon cancer cell lines. Cells were split and drugs were refreshed every 72 hours for the indicated number of days before plating (pretreatment) and were retreated and replated a final time at day 0 of IncuCyte measurements. Data are representative of three biological replicates, and the means ± SEM ($n = 12$ images for HCT116, HCT15, and Colo205; $n = 9$ images for SW620 and Caco2 per time point and treatment) of technical replicates from a single experiment is shown. (**B**) Representative brightfield images of Apc$^{\mathrm{Min}/+}$ mouse intestinal adenoma ex vivo tumoroids treated for 21 days. Vehicle or inhibitors were refreshed every 72 to 96 hours, and tumoroids were split every 7 to 9 days. (**C**) Tumoroid phenotype after treatment. Types 1 and 2 are normal and viable, while types 3 and 4 are unhealthy with progressive loss of normal cyst-like morphology. Examples of each morphology phenotype are shown in fig. S3H. Data are the percentage of total tumoroids evaluated from $n = 35$ to 66 organoids per treatment group. See also fig. S3.

is now appreciated to demarcate an intermediate "I" compartment of the genome that sits between the active "A" compartment and inactive "B" compartment (*61*, *62*). In addition, these I compartments are enriched for the transition between early and late replication timing (fig. S4J) (*63*). We used 16-phase Repli-Seq data for HCT116 (*64*) to determine how H3K27me3 changes following treatment in the context of replication timing phases. Consistent with the notion that H3K27me3 is enriched at transitional regions, H3K27me3 depletion was enriched for the phases of replication timing that denote a transition from early replication to late replication (Fig. 4D, left). Collectively, these data demonstrate that TAZ (with or without DAC) depletes H3K27me3 at genomic regions known to be regulated by PRC2.

From prior work, we hypothesized that H3K27me3 would replace DNA methylation as a repressive epigenetic signal when genomes are hypomethylated (*28*, *30*, *33*, *65*, *66*). Consistent with this hypothesis, Western blot (fig. S1B) and siQ-ChIP (Fig. 4, A and B) analyses showed that H3K27me3 levels globally increased after DNMTi treatment in a dose-dependent manner. ChromHMM and Repli-Seq enrichment analyses demonstrated that increases in H3K27me3 occurred at Polycomb repressive–regulated regions (EnhBiv, ReprPC1, ReprPC2, and ReprPCWk) and intermediate replication timing phases, respectively (Fig. 4, C and D, right). While single-agent TAZ and combination treatments did not induce significant losses of H3K27me3 in "weak" Polycomb regions (ReprPCWk) (Fig. 4C, left), the increases in H3K27me3 following DAC treatment did occur in these regions (Fig. 4C, right).

The prevailing view in the field is that H3K27me3 and DNA methylation genomic distributions are mutually exclusive. However, experiments coupling H3K27me3 ChIP-seq with bisulfite sequencing of immunoprecipitated fragments identified genomic regions where these two epigenetic modifications co-occur and showed that this dual repression epigenetic signature is more prevalent in cancer cells (*39*, *67*, *68*). By global DNA methylation analysis on EPIC arrays, low-dose DAC in single-agent and combination treatments effectively reduced DNA methylation levels by ~15% (figs. S1G and

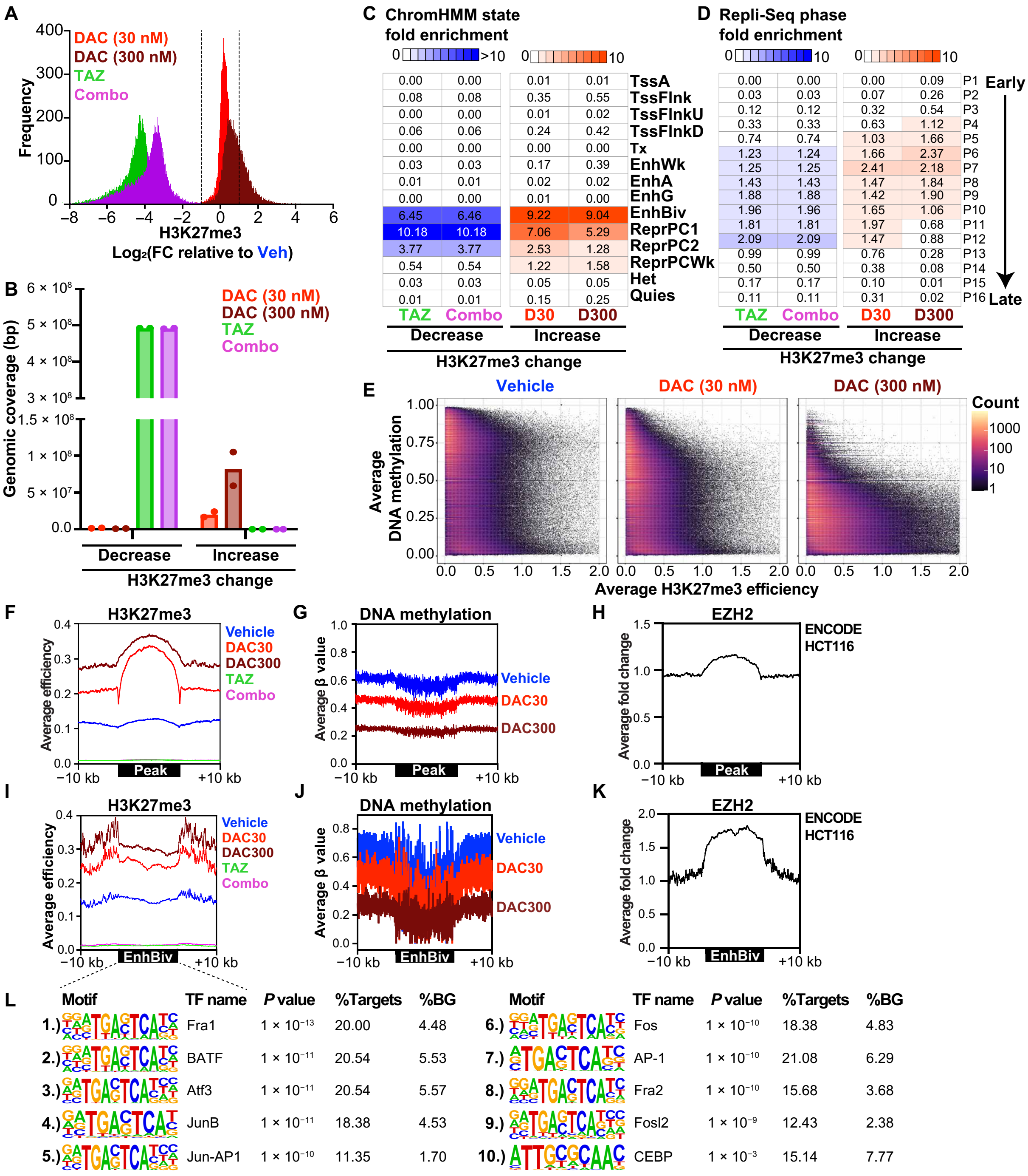

C ChromHMM state fold enrichment

	Decrease		Increase	
	TAZ	Combo	D30	D300
TssA	0.00	0.00	0.01	0.01
TssFlnk	0.08	0.08	0.35	0.55
TssFlnkU	0.00	0.00	0.01	0.02
TssFlnkD	0.06	0.06	0.24	0.42
Tx	0.00	0.00	0.00	0.00
EnhWk	0.03	0.03	0.17	0.39
EnhA	0.01	0.01	0.02	0.02
EnhG	0.00	0.00	0.01	0.00
EnhBiv	6.45	6.46	9.22	9.04
ReprPC1	10.18	10.18	7.06	5.29
ReprPC2	3.77	3.77	2.53	1.28
ReprPCWk	0.54	0.54	1.22	1.58
Het	0.03	0.03	0.05	0.05
Quies	0.01	0.01	0.15	0.25

H3K27me3 change

D Repli-Seq phase fold enrichment

	Decrease		Increase	
	TAZ	Combo	D30	D300
P1 Early	0.00	0.00	0.00	0.09
P2	0.03	0.03	0.07	0.26
P3	0.12	0.12	0.32	0.54
P4	0.33	0.33	0.63	1.12
P5	0.74	0.74	1.03	1.66
P6	1.23	1.24	1.66	2.37
P7	1.25	1.25	2.41	2.18
P8	1.43	1.43	1.47	1.84
P9	1.88	1.88	1.42	1.90
P10	1.96	1.96	1.65	1.06
P11	1.81	1.81	1.97	0.68
P12	2.09	2.09	1.47	0.88
P13	0.99	0.99	0.76	0.28
P14	0.50	0.50	0.38	0.08
P15	0.17	0.17	0.10	0.01
P16 Late	0.11	0.11	0.31	0.02

H3K27me3 change

L

Motif	TF name	*P* value	%Targets	%BG
1.)	Fra1	1×10^{-13}	20.00	4.48
2.)	BATF	1×10^{-11}	20.54	5.53
3.)	Atf3	1×10^{-11}	20.54	5.57
4.)	JunB	1×10^{-11}	18.38	4.53
5.)	Jun-AP1	1×10^{-10}	11.35	1.70
6.)	Fos	1×10^{-10}	18.38	4.83
7.)	AP-1	1×10^{-10}	21.08	6.29
8.)	Fra2	1×10^{-10}	15.68	3.68
9.)	Fosl2	1×10^{-9}	12.43	2.38
10.)	CEBP	1×10^{-3}	15.14	7.77

Fig. 4. Increased levels of H3K27me3 are associated with DAC-induced DNA hypomethylation at genomic regions poised with EZH2. (**A**) Histograms of $\text{Log}_2(\text{FC})$ in H3K27me3 efficiency relative to vehicle-treated samples. Combo is 1 μM TAZ plus 30 nM DAC. $\text{Log}_2(\text{FC})$ is averaged across biological duplicates. Dashed lines indicate the threshold for H3K27me3 signal considered significantly different from vehicle ($|\text{Log}_2\text{FC}| \geq 1$). (**B**) Genomic coverage (in base pairs) of significantly altered regions of H3K27me3 efficiency ($|\text{Log}_2\text{FC}| \geq 1$) relative to vehicle. (**C** and **D**) Fold enrichment overlap analysis of lost (TAZ/combo) and gained [30 nM DAC (DAC30)/300 nM DAC (DAC300)] H3K27me3 efficiency regions relative to vehicle ($|\text{Log}_2\text{FC}| \geq 1$) in relation to (C) ChromHMM states and (D) replication timing (Repli-Seq) phases from HCT116. (**E**) Density scatterplots of average H3K27me3 efficiency (measured by siQ-ChIP-seq) versus average DNA methylation (measured by EM-seq of siQ-ChIP-seq fragments) for the indicated treatment conditions following 72-hour exposure in HCT116. Average values are plotted from biological duplicates across 100-bp bins. (**F** to **H**) Average profiles for (F) H3K27me3 efficiency, (G) DNA methylation, and (H) EZH2 occupancy at conserved genomic regions that show increased H3K27me3 levels following 30 nM DAC treatment ($n = 3223$ peaks). (**I** to **K**) Average profiles for (I) H3K27me3 efficiency, (J) DNA methylation, and (K) EZH2 occupancy at conserved bivalent enhancers (EnhBiv) that show increased H3K27me3 following 30 nM DAC treatment ($n = 185$ enhancer regions). (**L**) HOMER transcription factor (TF) motif enrichment analysis of EnhBiv regions that show increased H3K27me3 after 30 nM DAC treatment. %Targets: percentage of given regions with indicated motif; %BG: percentage of the queried representative background with indicated motif. See also fig. S4.

S4B). As the EPIC array provides limited coverage of Polycomb repressive genomic regions, we used a similar technique by coupling siQ-ChIP to enzymatic methyl (EM) sequencing (ChIP-EM-seq) to generate high-coverage maps of the quantitative distributions of DNA methylation and H3K27me3 in cells exposed to DAC, which allowed us to define the relationship between these epigenetic modifications on the same chromatin fragments (fig. S4, D to G). Consistent with DAC-induced global accumulation of H3K27me3 (fig. S1B), ChIP-EM-seq showed DAC single-agent treatment effectively decreased DNA methylation while increasing H3K27me3 in a dose-dependent manner (Fig. 4E). In addition, while H3K27me3 and DNA methylation do appear to largely anticorrelate with each other, many instances exist where these modifications do coexist in the genome (fig. S4G).

Next, we focused on those genomic regions that consistently gained H3K27me3 after low-dose DAC treatment and averaged H3K27me3 levels over the start and stop coordinates of these regions (Fig. 4F and fig. S4K). Notably, these peaks started with low levels of H3K27me3 in vehicle-treated controls and significantly increased H3K27me3 in a dose-dependent manner after DAC treatment. These genomic regions seem to be primed for an "epigenetic switch," replacing DNA methylation with H3K27me3 after DAC treatment (Fig. 4, F and G). ENCODE ChIP-seq data for HCT116 cells show that EZH2 is enriched across these regions (Fig. 4H and fig. S4L), suggesting that PRC2 is "poised" for H3K27me3 deposition in these regions when the genome is hypomethylated by DAC treatment. Given the localization of hypomethylated differentially methylated regions (DMRs) at intronic, genic, and distal intergenic regions (fig. S4C), we further found that bivalent enhancers (regulatory elements marked by H3K4me1 and H3K27me3) follow the same epigenetic switch pattern (Fig. 4, I and J). These enhancers also appear to be poised with EZH2 to mediate H3K27me3 accumulation (Fig. 4K). Notably, HOMER motif analysis revealed a significant enrichment for activating protein 1 (AP-1) (Jun/Fos) binding motifs at these bivalent enhancers (Fig. 4L). Collectively, our epigenomic analyses suggest that combination treatment effectively reduces DNA methylation, blocks H3K27me3 deposition, and potentially opens up enhancers for AP-1 transcription factors.

EZH2i enhances DNMTi-driven transcriptional responses after prolonged treatment

Substantial measurable alterations to the global epigenome were observed as early as 3 days after treatment (fig. S1, B and G), but antiproliferative effects of combined DNMT and EZH2 inhibition were most prominent with extended treatment (Fig. 3A). Therefore, we next analyzed the global transcriptional response to the DAC plus TAZ combination following both prolonged (6-day) and acute (3-day) treatments. Single-agent DAC and TAZ drug treatments up-regulated hundreds of protein-coding (PC) genes on their own (Fig. 5, A to D). Combined DAC and TAZ treatments further enhanced the transcriptional up-regulation of these single agent–responsive genes (fig. S5, A to D) while stimulating more than 600 additional PC genes following both prolonged (Fig. 5, A and B) and acute treatments (Fig. 5, C and D). Many of the up-regulated genes in the 6-day treatment protocol were already expressed by day 3 (fig. S5E). Prolonged treatment revealed that TEs were also significantly up-regulated with single-agent treatments and, to a much greater extent, with the combination (Fig. 5A). Notably, TE expression following acute exposure was unique to combination treatment and was increased nearly 10-fold after prolonged drug exposure (Fig. 5C), indicating that activation of TEs requires sustained, prolonged treatment with the DNMTi and EZH2i combination when DNMTis are used at a low dose. These data suggest that viral mimicry and an innate immune response can be induced with combined DAC and TAZ treatment and enhanced with prolonged drug exposure.

Consistent with previous studies of DNMT inhibition in colon, breast cancer (BRCA), and ovarian cancer, combination epigenetic therapy significantly up-regulated pathways involved in extracellular matrix organization (*23*, *69*) and a viral mimicry-associated innate immune response (*6*, *7*, *23*) (Fig. 5E and fig. S5, F and G). Although up-regulation was the predominate direction of the transcriptional response, gene set enrichment analysis (GSEA) revealed that MYC and its targets were consistently down-regulated with combination treatment (Fig. 5E and fig. S5H), a response previously reported with DNMTi and histone deacetylase (HDAC) inhibitor combination treatment (*70*, *71*). Together, prolonged EZH2 inhibition with DNMT inhibition strongly enhanced the appreciated transcriptional reprogramming effects of DNMT inhibition alone, including therapeutically actionable effects of innate immune pathway activation and MYC pathway down-regulation.

Combined DNMTi and EZH2i up-regulate calcium-calcineurin-NFAT pathway transcriptional signatures and PRC2 target genes

As was observed at the prolonged treatment time point, GSEA of transcriptional signatures unique to acute combination treatment revealed induction of innate immune response pathways, extracellular matrix organization, and known PRC2 target genes (Fig. 5F and fig. S5I). Notably, among the most significantly up-regulated pathways following acute combination treatment were gene sets associated with T cell activation and calcium signaling (Fig. 5, F and G). Converging on this observation and from motif analysis described in Fig. 4, I to L, AP-1 (composed of JUN/FOS), myocyte enhancer factor 2 (MEF2), and NFAT target genes were among the most enriched gene sets up-regulated with acute combination treatment (Fig. 5H), and expression of these transcription factors was stimulated by the drug combination (Fig. 5I). Moreover, many NFAT target genes, genes associated with T cell receptor signaling, and genes involved in calcium signaling were induced from a silenced state following acute combination treatment (Fig. 5J). Transcriptional up-regulation of *IFI27* (interferon α-inducible protein-27; a downstream component of the viral mimicry pathway and a combo-responsive gene) and genes in the calcium-calcineurin-NFAT signaling pathway that respond to the drug combination in HCT116 cells were validated in several additional colon cell lines and three renal cell carcinoma cell lines (fig. S6, A and B), demonstrating conservation of this mechanism across a range of solid tumor types. Collectively, acute combination treatment stimulated many of the transcriptional responses (i.e., TE expression and innate immune pathway activation) that become predominant after prolonged treatment. Acute combination treatment also significantly up-regulated transcription of calcium signaling, downstream calcium-associated transcription factors, and their targets, suggesting that changes to the chromatin environment mediated by the drug combination facilitate the activation of this pathway.

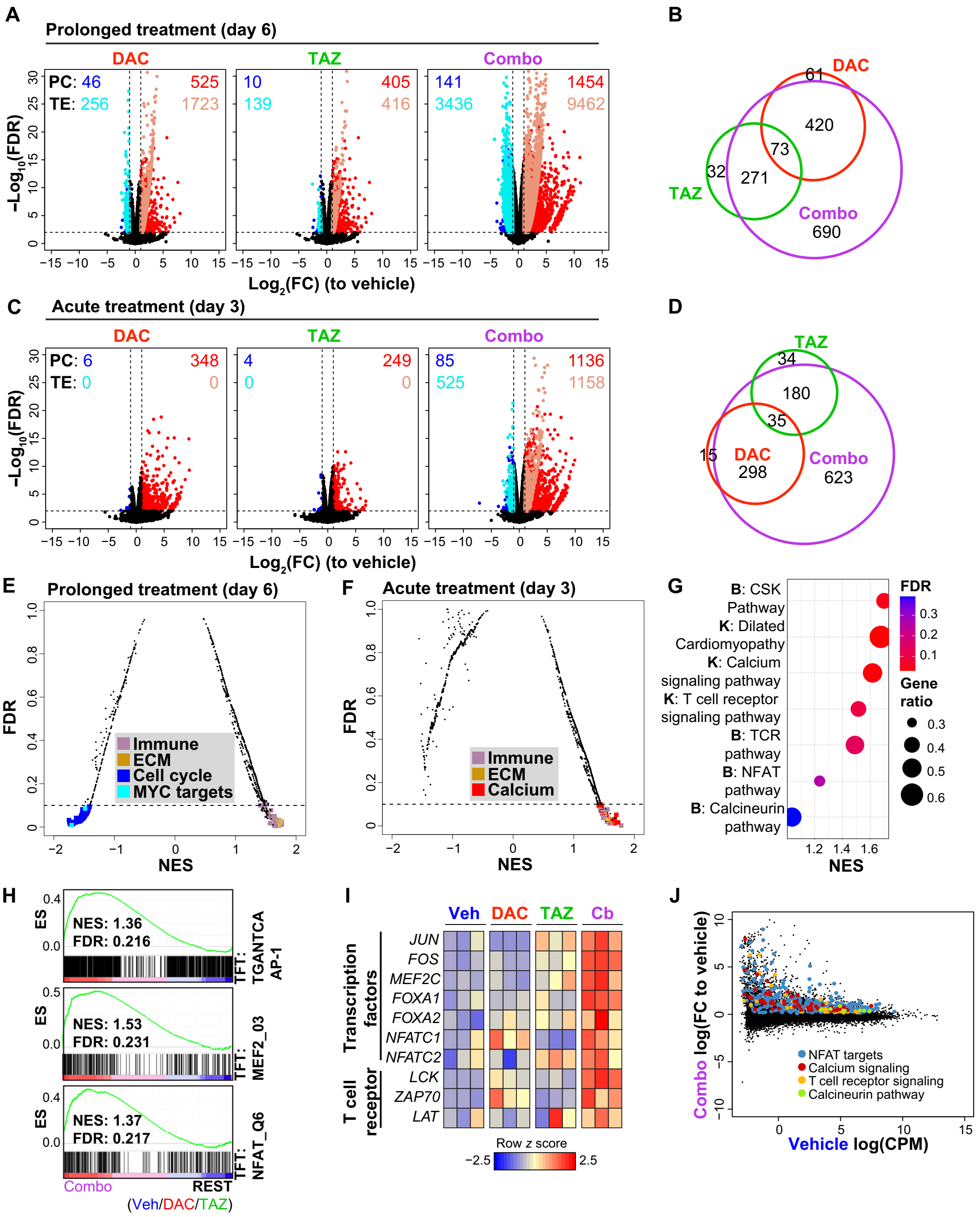

Fig. 5. TAZ enhances transcriptional responses associated with DNMT inhibition. (**A**) Volcano plots for PC genes and TE expression from total RNA sequencing (RNA-seq) of indicated treatments (DAC, 30 nM; TAZ, 1 μM) relative to vehicle in HCT116 following 6 days of treatment. Data points are plotted as averages from three biological replicates. PC and TE transcripts with significance threshold of $\log_2(FC) \geq 1.0$ and false discovery rate (FDR) ≤ 0.01 are colored points. Black points do not meet threshold conditions. (**B**) Venn diagram of overlapping PC genes significantly up-regulated by treatments from (A). (**C**) Volcano plots for PC genes and TE expression from total RNA-seq among indicated treatments relative to vehicle [DMSO/phosphate-buffered saline (PBS)] after 72 hours of treatment. Data points are plotted as averages from three biological replicates. (**D**) Venn diagram of overlapping PC genes significantly up-regulated treatments from (C). (**E**) GSEA summary for HALLMARK, REACTOME, Kyoto Encyclopedia of Genes and Genomes (KEGG), and BioCarta gene sets in combo treatment versus REST (vehicle/DAC/TAZ) after 6 days of treatment. Gene sets that meet a significance threshold of FDR ≤ 0.1 are colored. NES, normalized enrichment score; ECM, extracellular matrix. (**F**) GSEA summary as described in (E) following 72 hours of treatment. (**G**) GSEA summary of up-regulated BioCarta (B) and KEGG (K) gene sets that relate to calcium signaling. Gene ratio is the ratio of the core enrichment genes for the indicated gene set divided by the total number of genes present in the gene set. TCR, T cell receptor. (**H**) GSEA analysis of combo versus REST for transcription factor target (TFT) genes sets. ES, enrichment score. (**I**) Row *z* score heatmaps of significantly up-regulated transcription factors and T cell receptor–associated genes following combination inhibitor treatment for 72 hours. Cb, Combo. (**J**) MA plot for differentially expressed genes in combo following 72-hour treatment. Core enrichment genes identified from GSEA analysis are colored. See also figs. S5 and S6.

Reduced DNA methylation and H3K27me3 at promoters associate with acute transcriptional responses to the drug combination

We next sought to define the relationship between chromatin modification changes and transcriptional responses after single-agent and combined treatments. To do this, we integrated siQ-ChIP (H3K27me3), EM-seq (DNA methylation), and available ENCODE data for EZH2, H3K4me3, and H3K27 acetylation (H3K27ac) occupancy across promoters of genes that were significantly up-regulated following acute drug exposure (Fig. 5D and fig. S5D). Genes up-regulated in response to DAC (Fig. 5D, all genes in red circle) had low levels of H3K27me3, H3K4me3, and H3K27ac, and high levels of DNA methylation across their Transcription Start Sites (TSSs) in vehicle-treated HCT116 cells (Fig. 6, A and B, and fig. S7A). H3K27me3 levels were marginally elevated in this gene set following DAC treatment, consistent with a lack of EZH2 association (Fig. 6A and fig. S7A). Genes up-regulated in response to TAZ (Fig. 5D, all genes in green circle) had high levels of H3K27me3 across their promoters and DNA hypomethylation at their TSSs (Fig. 6, A and B, and fig. S7A). Notably, TAZ-responsive genes appear to be in a poised bivalent state with both EZH2 and H3K4me3 flanking the TSS. Unlike DAC-responsive genes, TAZ-responsive genes showed elevated H3K27me3 following DAC treatment, suggesting that while these genes are primarily silenced by H3K27me3, DNA hypomethylation stimulates poised EZH2 to deposit additional H3K27me3 to maintain a repressed state. The dynamics of epigenetic regulation were also evident across gene bodies of drug-induced up-regulated genes (fig. S7B).

We next focused on the epigenetic architecture surrounding promoters of genes that exclusively responded to the combination treatment (Fig. 5D, $n = 623$ genes in purple circle). Unlike single agent–responsive genes, combination only–responsive genes did not demonstrate a clear overarching epigenetic regulatory mechanism (fig. S7A). Rather, genes exclusively up-regulated by the combination treatment could be further subdivided into three groups based on promoter architecture of histone PTMs associated with active transcription (Fig. 6, C and D, and fig. S7C). Approximately half of these genes were not marked by H3K27ac or H3K4me3. The remainder were marked by H3K4me3 alone or in combination with H3K27ac (Fig. 6, C and D, and fig. S7C).

The expression of DAC- and TAZ-responsive genes is associated with drug-induced losses of DNA methylation and H3K27me3, respectively; this was also observed within the combination treatment–responsive gene cluster lacking H3K4me3 and H3K27ac, where loss of both DNA methylation and H3K27me3 correlated with gene expression (Fig. 6E, left column). These genes were primarily found in Polycomb-regulated regions of the genome (EnhBiv, ReprPC1, and ReprPCWk) and in the transition regions from early to late replication timing (Fig. 6, F and G). Significantly, these genes were enriched not only for known Polycomb target genes in embryonic stem cells (Fig. 6H) but also for genes that contain AP-1 (Jun/Fos) and NFAT transcriptional factor binding motifs (Fig. 6I).

Similar to the TAZ-responsive gene cluster, the combination treatment cluster marked by H3K4me3 had bivalent promoter architecture with H3K27me3 and EZH2 across the TSS (Fig. 6E, middle column). These bivalent genes were also found in regions of the genome known to be associated with Polycomb regulation (EnhBiv, ReprPC1, and ReprPC2) and the transition regions from early to late replication timing (Fig. 6, F and G). Consistent with a bivalent promoter architecture, this subgroup of genes was significantly enriched for known Polycomb target genes in embryonic stem cells (Fig. 6H) but did not demonstrate strong enrichment for transcription factor binding sites in the promoter (Fig. 6I).

Last, the combination treatment cluster marked by H3K4me3 and H3K27ac showed no significant changes in H3K27me3 (and had the lowest H3K27me3 signal among all combination only–responsive genes) and the deepest depletion of DNA methylation at the TSS among all treatments, which are epigenetic signatures consistent with active gene transcription (Fig. 6E, right column). Genes in this subcategory were already active in vehicle-treated HCT116 cells, and they were further up-regulated by the combination treatment (fig. S7D), suggesting that up-regulation of these genes is a downstream effect of activation of other upstream genes and not dependent on changes in local epigenetic architecture induced by the drug combination. Consistent with this notion, these genes were not located in known Polycomb-regulated regions and, instead, were enriched for known active regions of the genome and earlier replication timing phases (Fig. 6, F and G). In addition, these genes were not enriched for known Polycomb targets (Fig. 6H); however, they did demonstrate enrichment for targets of AP-1 (Jun/Fos) and NFAT transcription factor binding motifs (Fig. 6I), suggesting that up-regulation of these genes is a downstream effect of calcium signaling and associated transcription factor activation by the combination treatment.

Transcriptional activating effects of combined DNMTi and EZH2i require calcium-calcineurin-NFAT signaling

Our studies to this point show that combined DAC and TAZ treatment up-regulates genes related to the calcium-calcineurin-NFAT signaling pathway (Fig. 5, F to J) and that genomic loci that undergo an epigenetic switch from DNA methylation to H3K27me3 when treated with DAC are enriched for AP-1 and NFAT binding motifs (Fig. 4, I to L). This is consistent with prior work in colon cancer cell lines showing that *SFRP1* can be activated by treating cells with cardiac glycosides that stimulate calcium signaling (*72*). When we treated HCT116 cells with various calcium signaling antagonists, the DAC and TAZ combination was no longer able to fully reactivate *SFRP1* (fig. S8A).

Cyclosporin A (CsA) was most effective at blocking *SFRP1* expression and did so in a dose-dependent manner (Fig. 7A and fig. S8A). CsA inhibits calcineurin, a calcium/calmodulin-dependent serine/threonine kinase that promotes NFAT translocation to the nucleus by dephosphorylating a nuclear localization signal (*73*). The 5 μM CsA treatment used here robustly blocked both *SFRP1* expression (Fig. 7A) and, using an NFAT1 antibody whose specificity was verified by NFAT1 knockdown (fig. S8B), NFAT accumulation in the nucleus (fig. S8C). Although CsA can induce G_0-G_1 cell cycle arrest (*74*), this concentration had no noticeable effects on the fraction of HCT116 in each cell cycle phase (fig. S8D). It also did not prevent or interfere with the direct epigenetic activity of TAZ or DAC (Fig. 7, B and C, and fig. S8E). Collectively, these data suggested that combined DAC and TAZ treatment activates genes through the calcium-calcineurin-NFAT pathway.

To test this hypothesis, we next performed RNA sequencing (RNA-seq) on HCT116 acutely exposed to the DAC and TAZ combination in the presence of CsA. CsA treatment alone down-regulated the expression of a limited number of PC genes and TEs (233 and 838, respectively) (Fig. 7D, left), while also preventing the expression of

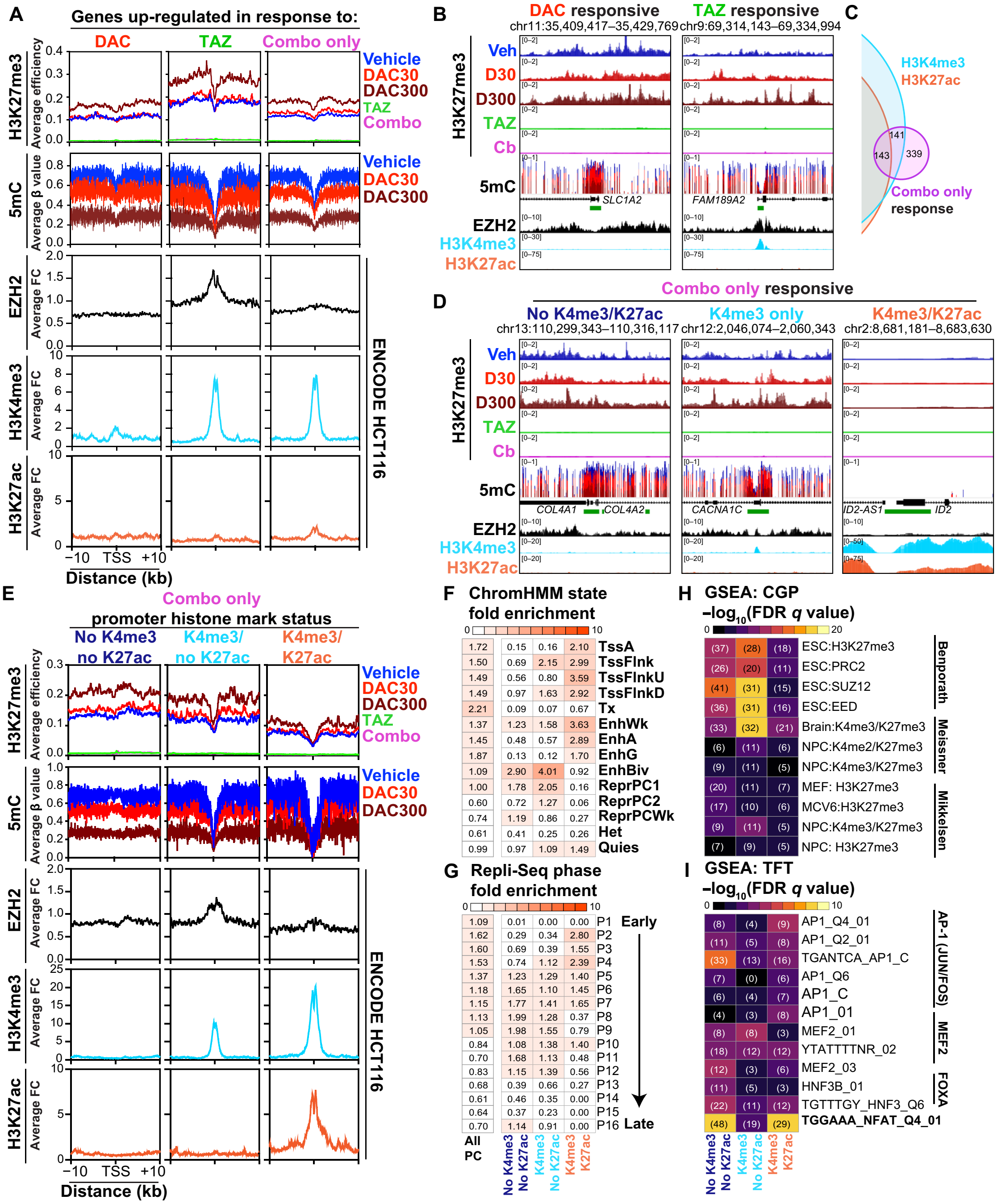

F ChromHMM state fold enrichment

All PC	No K4me3 No K27ac	K4me3 No K27ac	K4me3 K27ac	
1.72	0.15	0.16	2.10	TssA
1.50	0.69	2.15	2.99	TssFlnk
1.49	0.56	0.80	3.59	TssFlnkU
1.49	0.97	1.63	2.92	TssFlnkD
2.21	0.09	0.07	0.67	Tx
1.37	1.23	1.58	3.63	EnhWk
1.45	0.48	0.57	2.89	EnhA
1.87	0.13	0.12	1.70	EnhG
1.09	2.90	4.01	0.92	EnhBiv
1.00	1.78	2.05	0.16	ReprPC1
0.60	0.72	1.27	0.06	ReprPC2
0.74	1.19	0.86	0.27	ReprPCWk
0.61	0.41	0.25	0.26	Het
0.99	0.97	1.09	1.49	Quies

G Repli-Seq phase fold enrichment

All PC	No K4me3 No K27ac	K4me3 No K27ac	K4me3 K27ac	
1.09	0.01	0.00	0.00	P1 Early
1.62	0.29	0.34	2.80	P2
1.60	0.69	0.39	1.55	P3
1.53	0.74	1.12	2.39	P4
1.37	1.23	1.29	1.40	P5
1.18	1.65	1.10	1.45	P6
1.15	1.77	1.41	1.65	P7
1.13	1.99	1.28	0.37	P8
1.05	1.98	1.55	0.79	P9
0.84	1.08	1.38	1.40	P10
0.70	1.68	1.13	0.48	P11
0.83	1.15	1.39	0.56	P12
0.68	0.39	0.66	0.27	P13
0.61	0.46	0.35	0.00	P14
0.64	0.37	0.23	0.00	P15
0.70	1.14	0.91	0.00	P16 Late

H GSEA: CGP −log10(FDR q value)

No K4me3 No K27ac	K4me3 No K27ac	K4me3 K27ac		
(37)	(28)	(18)	ESC:H3K27me3	Benporath
(26)	(20)	(11)	ESC:PRC2	
(41)	(31)	(15)	ESC:SUZ12	
(36)	(31)	(16)	ESC:EED	
(33)	(32)	(21)	Brain:K4me3/K27me3	Meissner
(6)	(11)	(6)	NPC:K4me2/K27me3	
(9)	(11)	(5)	NPC:K4me3/K27me3	
(20)	(11)	(7)	MEF: H3K27me3	Mikkelsen
(17)	(10)	(6)	MCV6:H3K27me3	
(9)	(11)	(5)	NPC:K4me3/K27me3	
(7)	(9)	(5)	NPC: H3K27me3	

I GSEA: TFT −log10(FDR q value)

No K4me3 No K27ac	K4me3 No K27ac	K4me3 K27ac		
(8)	(4)	(9)	AP1_Q4_01	AP-1 (JUN/FOS)
(11)	(5)	(8)	AP1_Q2_01	
(33)	(13)	(16)	TGANTCA_AP1_C	
(7)	(0)	(6)	AP1_Q6	
(6)	(4)	(7)	AP1_C	
(4)	(3)	(8)	AP1_01	
(8)	(8)	(3)	MEF2_01	MEF2
(18)	(12)	(12)	YTATTTTNR_02	
(12)	(3)	(6)	MEF2_03	
(11)	(5)	(3)	HNF3B_01	FOXA
(22)	(11)	(12)	TGTTTGY_HNF3_Q6	
(48)	(19)	(29)	**TGGAAA_NFAT_Q4_01**	

Fig. 6. DAC plus TAZ combination treatment promotes acute transcriptional responses by inducing loss of DNA methylation and H3K27me3 at promoters. (**A**) Integrative epigenomic analysis (rows) centered on the TSS of genes up-regulated by the indicated treatments (columns) in HCT116 following 72-hour treatment with 30 nM DAC and 1 μM TAZ. Average profiles for H3K27me3 and DNA methylation (5mC) were determined from biological duplicate siQ-ChIP-seq and EM-seq measurements, respectively. EZH2, H3K4me3, and H3K27ac profiles were determined from publicly available ENCODE data for HCT116. (**B**) Representative browser shots for a DAC-responsive locus (*SLC1A2)* and a TAZ-responsive locus (*FAM189A2*) demonstrating patterns observed in average profiles from (A). (**C**) Venn diagram of genes up-regulated by combination treatment overlapped with genes that contain activating histone PTMs (H3K4me3/H3K27ac) in the promoter (±1000 bp centered on TSS). Combo only–responsive genes are subdivided by the presence/absence of active histone PTMs in their promoters. (**D**) Representative browser shots for the different subdivisions of promoter architecture of combo only–responsive genes derived from (A) and (C). (**E**) Integrative epigenomic analysis (rows) centered on the TSSs of genes up-regulated by the combination inhibitor treatment only (combo only) subdivided by promoter histone PTM status from (C). Profiles derived as in (A). (**F** and **G**) Fold enrichment overlap analysis of genes up-regulated by combo only subdivided by the promoter histone PTM status with (D) ChromHMM states and (E) replication timing (Repli-Seq) phases in HCT116. (**H** and **I**) Hypergeometric overlap analysis of combo-only up-regulated genes subdivided by promoter histone PTM status with (H) GSEA C2: chemical and genetic perturbations related to known studies of PRC2 regulation and (F) GSEA C3: TFT. Heatmaps represent the significance of the overlap and number of genes in overlap provided in parentheses. See also fig. S7.

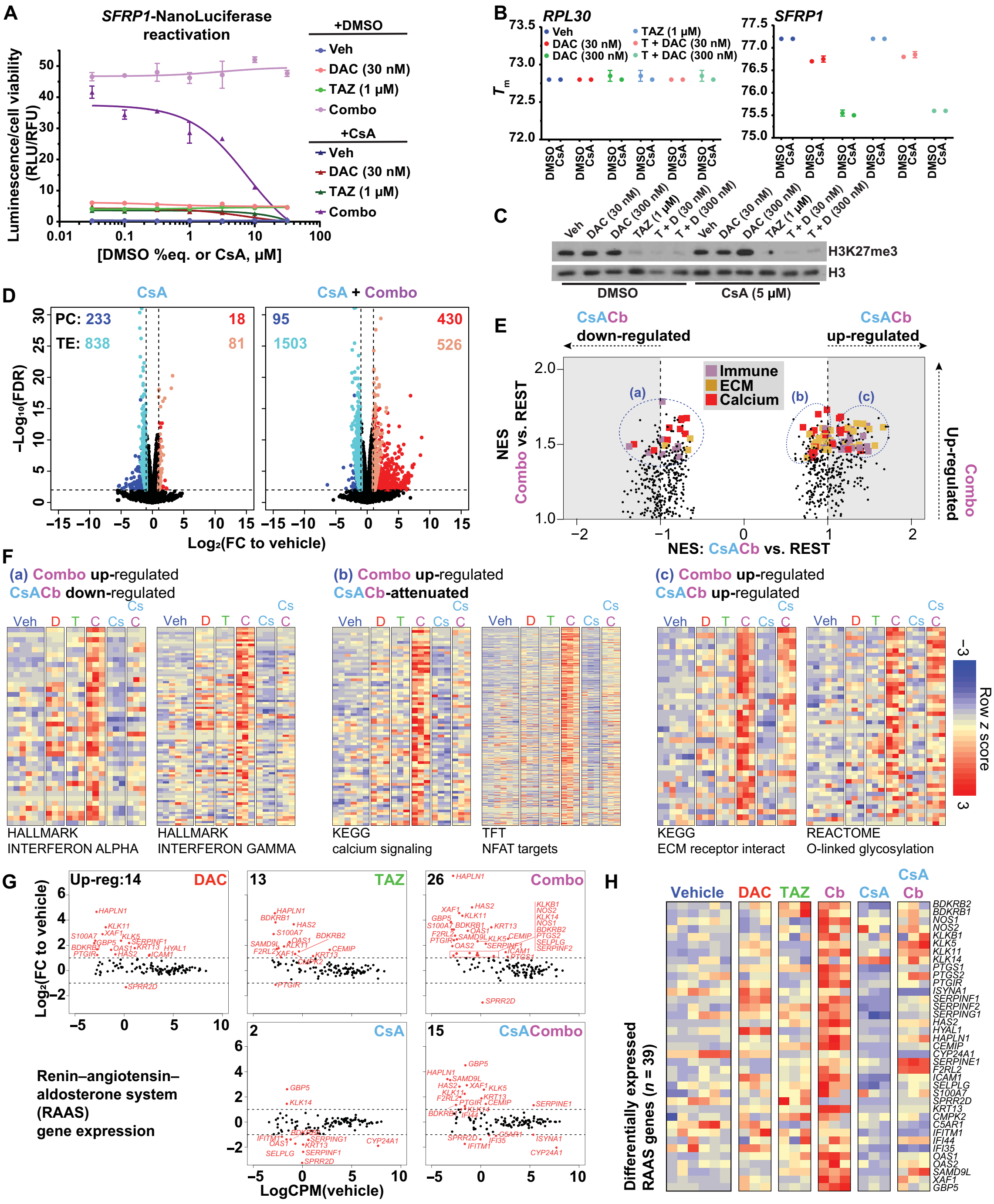

Fig. 7. The transcriptional activating effects of the DAC plus TAZ combination treatment require signaling through the calcium-calcineurin-NFAT pathway. (**A**) *SFRP1*-NLuc reporter activity measurements following treatments with or without CsA. RLU are normalized to RFU from CellTiter-Fluor viability assay. Data are representative of three biological replicates, and the means ± SD of technical triplicates from a single experiment is shown. (**B**) High-resolution melt analysis of HCT116 cells treated with vehicle, DAC, TAZ, or combo in presence or absence of CsA. *RPL30*, unmethylated control gene; *SFRP1*, methylated CGI promoter. Data are representative of two biological replicates, and the means ± SD of technical duplicates from a single experiment is shown. (**C**) Western blot analysis for H3K27me3 from HCT116 treated with TAZ and/or DAC in presence of CsA. (**D**) Volcano plots for PC genes and TEs in HCT116 following treatment. Data points are plotted as averages from three biological replicates. Transcripts with significance threshold of $\log_2(\mathrm{FC}) \geq 1.0$ and FDR ≤ 0.01 are colored. (**E**) Comparative GSEA analysis of HALLMARK, BioCarta, KEGG, and REACTOME gene sets between combination treatment without and with CsA. Comparative responses are classified as follows (circled in blue): (a) combo up-regulated, CsACb down-regulated; (b) combo up-regulated, CsACb-attenuated; and (c) combo up-regulated, CsACb up-regulated. (**F**) Row *z* score heatmaps of core enrichment genes from GSEA analysis of combo versus REST for the indicated gene sets in (E). (**G**) MA plots for gene expression associated with the RAAS across the different treatments. (**H**) Heatmap of normalized counts for significantly differentially expressed ($|\mathrm{Log}_2\mathrm{FC}| \geq 1.0$) RAAS-associated genes. Color scale from (F) applies. All treatments for 72 hours [DAC, 30 nM in (D) to (H); TAZ, 1 μM; CsA, 5 μM]. See also fig. S8.

many of the genes responsive to combination treatment (Figs. 4C, volcano plot on right, and 7D, right). Addition of CsA to the combination treatment blocked or attenuated many of the immune and calcium signaling responses [Fig. 7, E and F (a and b), and fig. S8F] observed following acute treatment (Fig. 5F), while maintaining up-regulation of extracellular matrix associated pathways [Fig. 7, E and F (c)]. Consistent with calcineurin being a major target of CsA, genes involved in calcium signaling were not induced by the epigenetic drug combination when CsA was coadministered [Fig. 7F (b)]. In addition, CsA attenuated the expression of NFAT target genes induced by the DAC and TAZ combination [Fig. 7F (b)]. Furthermore, CsA attenuated the up-regulation of *IFI27* and many of these calcium-calcineurin-NFAT genes that are induced by the epigenetic combination in renal and lung cancer cell lines, demonstrating conservation of this mechanism across several solid tumor types (fig. S8G).

The effect of CsA on TE induction by the epigenetic drug combination prompted us to consider whether calcium signaling pathway induction was needed for stimulating the expression of genes associated with an innate immune response to viral infection. Moreover, we link another key set of genes associated with inflammation, those associated with the renin–angiotensin–aldosterone system (RAAS) pathway. RAAS, when abnormally overactive, produces a series of severe tissue inflammatory consequences (*75*). Both increases in innate immune and RAAS genes were attenuated when calcium pathway signaling was blocked with CsA [Fig. 7, F (a) to H]. Collectively, our data support that the combination of DAC and TAZ induces a significant innate immune response that is dependent on calcium-calcineurin-NFAT signaling.

Transcriptional programs of calcium-calcineurin-NFAT pathway activation and the response to viral infection correlate in primary human colorectal adenocarcinomas

Last, we asked whether the link between transcriptional signatures of activated intracellular calcium signaling and an innate immune response was evident in biopsied human tumors. Before conducting this analysis, we identified a set of known innate immune response genes that consistently respond to low-dose AZA treatment across a panel of CRC cell lines and showed that these genes were responsive to combined DAC and TAZ treatment in HCT116 (Fig. 8A). Furthermore, the drug-induced expression of this gene set was dependent on calcium signaling (Fig. 8B) (*76*). We then clustered TCGA-COAD/READ (The Cancer Genome Atlas–colorectal adenocarcinoma/rectal adenocarcinoma) tumor samples based on this gene signature (*77*) and reproduced the separation of TCGA-COAD/READ samples into AZA immune gene set (AIM) "high" (high innate immune response) and AIM "low" (low innate immune response) clusters (Fig. 8C). COAD/READ samples that had an AIM high response also had high expression of core calcium signaling and RAAS gene sets (Fig. 8, D and E). The average calcium gene response, average innate immune response, and average RAAS response among individual samples were significantly correlated (Fig. 8, F to H). We performed a similar analysis using BRCA- and ovarian cancer–specific AIM gene sets (*76*) among TCGA-BRCA (fig. S9, A to F) (*77*) and TCGA-OV (fig. S9, G to L) (*78*) samples, respectively, and found that calcium signaling gene expression, RAAS genes, and the innate immune response were again highly correlated. Important to note is the lack of overlap among all queried gene sets (fig. S9, M to O). Collectively, these data show that the relationship between transcriptional programs of calcium-calcineurin-NFAT pathway activation and the response to virus infection that we causally linked in cultured colon cancer cells are also significantly correlated in biopsies of primary human tumors.

DISCUSSION

Therapeutic implications of combined DNMTi and EZH2i therapy

In this study, we show that compensatory accumulation of H3K27me3 after DAC treatment occurs primarily at distal Polycomb-regulated regions, preventing full transcriptional activation by DNMTis. This H3K27me3 accumulation therefore represents a therapeutic vulnerability in colon cancer cell lines that are normally insensitive to single-agent EZH2 inhibition. The unmet potential of DNMT inhibition therapy in patients with solid tumors underscores the importance of our findings.

Previous studies have attempted to exploit the cross-talk between DNA methylation and histone PTMs to treat cancer (*79*). For example, DNMTis have been combined with HDAC inhibitors as a way to increase chromatin accessibility and activate otherwise silenced TSGs (*44*, *80*, *81*). Combined DNMTi and HDAC inhibitor treatments have had mixed effects on clinical response rates and survival benefit compared to single-agent DNMTi treatment (*82*–*85*). HDAC inhibition was also associated with increased DNA damage, and this could explain some resultant pharmacodynamic antagonism with DNMT inhibition in cancer cell lines and patients (*17*, *86*–*89*).

Our study suggests that simultaneously targeting repressive lysine methylation signaling at H3K27, particularly using the clinically applied EZH2i TAZ, represents a different approach to augmenting the transcriptional and therapeutic effects of DNMT inhibition. Recent studies have begun examining the combinatorial use of DNMTi and EZH2i, with reports of cooperative therapeutic benefit that include reduced xenografted tumor or cell line growth, antineoplastic action, increased T cell infiltration, resensitization to immunomodulatory drugs, reexpression of silenced TSGs, and activation of the viral mimicry response (*10*, *35*, *37*–*40*, *79*). Consistent with these findings, perturbing DNA methylation, genetically or as a consequence of chemotherapy and metabolic perturbation, renders cancer cells sensitive to EZH2 inhibition (*34*, *36*). Our studies build from these reports, corroborating the combination antiproliferative effects of DNMT and EZH2 inhibition in colon cancer models while also providing in-depth analysis of the molecular effects of combined DNMT and EZH2 inhibition on the epigenome and transcriptome, the importance of which is discussed below. We also inform about the rational selection of epigenetic inhibitors used in clinical practice and provide rationale for expanding the use of EZH2is beyond tumor types that show a dependency on PRC2.

Immunomodulatory effects of combined DNMTi and EZH2i treatment

We and others found that TEs become activated after DNMT inhibition, which triggers a "viral mimicry response" mediated through dsRNA sensing and interferon signaling (*6*, *7*). Here, we show that TAZ enhances the DAC-induced expression of TEs and innate immune response pathways associated with viral mimicry. Activating antiviral response programs in tumors is associated with a better response to immunotherapy in preclinical models (*9*–*11*), and these

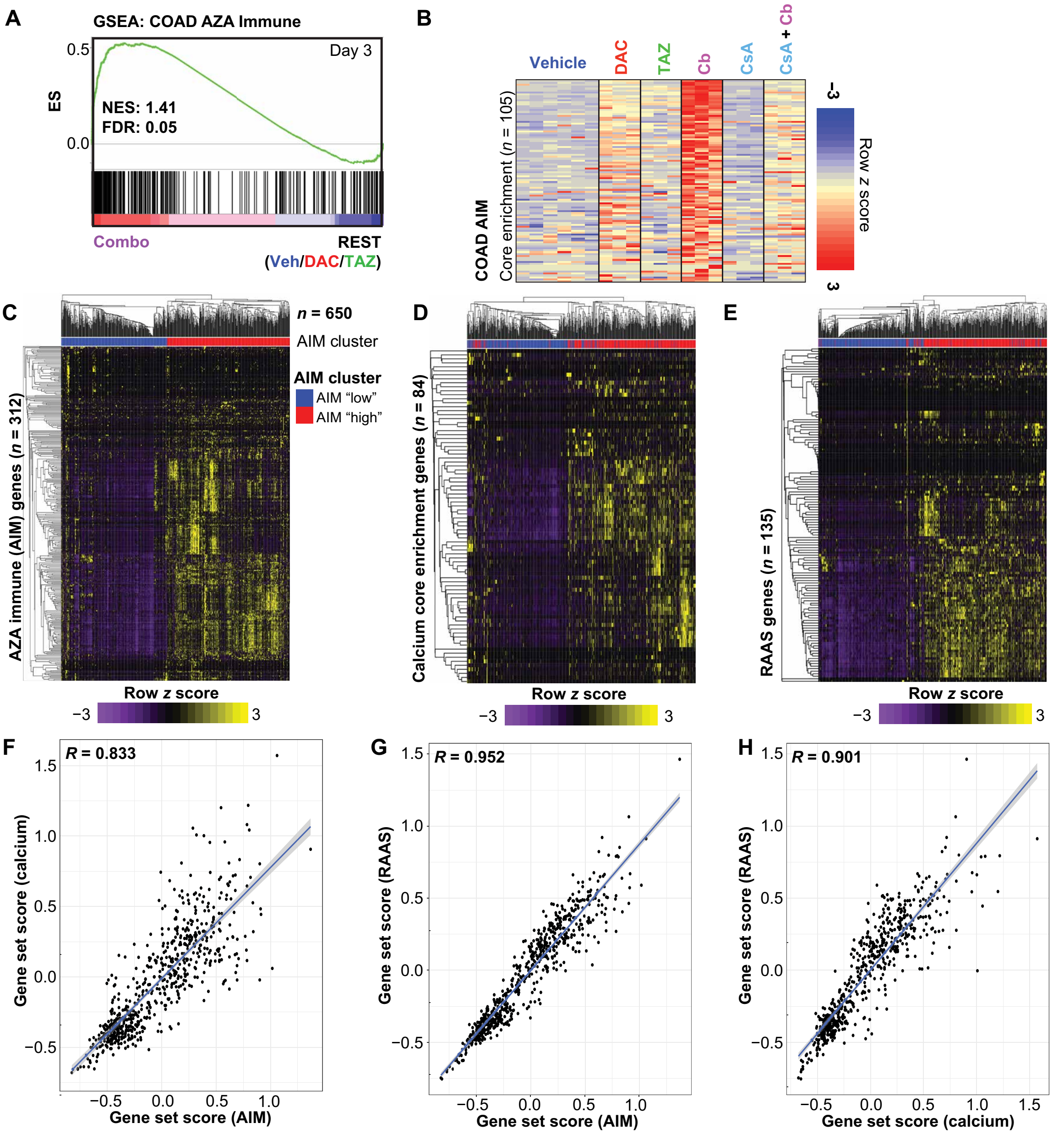

Fig. 8. TCGA-COAD/READ tumor biopsies with high innate immune response correlate with calcium signaling expression. (**A**) GSEA analysis of colon AIM genes for combo treatment versus REST (Veh/DAC/TAZ). (**B**) Row *z* score heatmaps of core enrichment genes from GSEA analysis in (A). (**C**) Supervised heatmap clustering of colon AIM gene expression among TCGA-COAD/READ tumor biopsies ($n = 650$ samples). AIM high cluster refers to samples that exhibit relative high expression of the colon AIM genes, and AIM low cluster refers to samples with relative low expression of the colon AIM genes. AIM cluster annotations are provided and carried through the subsequent analysis. (**D**) Supervised heatmap clustering of KEGG calcium signaling core enrichment (derived from 72-hour combo versus REST GSEA analysis) gene expression among TCGA-COAD/READ tumor samples. Annotations are carried from (C). (**E**) Supervised heatmap clustering of RAAS gene expression among TCGA-COAD/READ tumor samples. Annotations are carried from (C). (**F**) Pearson correlation analysis of AIM genes versus calcium genes among TCGA-COAD/READ samples. Each dot represents a sample. Gene set scores (for AIM and calcium) were calculated by averaging the *z* scores across the indicated gene set for individual samples. (**G**) Pearson correlation analysis of AIM genes versus RAAS genes among TCGA-COAD/READ samples. Analysis scheme described in (F) was followed. (**H**) Pearson correlation analysis of calcium genes versus RAAS genes among TCGA-COAD/READ samples. Analysis scheme described in (F) was followed. See also fig. S9.

data suggest future directions for testing whether DAC and TAZ treatments might improve tumor response to immunomodulating agents.

Combined DAC and TAZ treatment also transcriptionally upregulated components of the calcium-calcineurin-NFAT signaling pathway in numerous colon cancer cell lines and other solid tumor cancer cell lines (Fig. 5, F to J, and figs. S6 and S8G), but it is still unclear how this influences oncogenesis or solid tumor response to treatment (*72*, *90*, *91*). The calcium-calcineurin-NFAT pathway is instead primarily associated with T cell activation (*73*, *92*), and it is known that single-agent DNMTi or EZH2i therapy activates T cells and can improve immune modulation in cancer cells and in vivo cancer therapy models (*9*, *11*, *93*–*96*). Our data are consistent with a model whereby combined DNMTi and EZH2i treatment stimulates the tumor cell–extrinsic immune microenvironment, either by inducing viral mimicry or by activating the calcium-calcineurin-NFAT pathway. This may be of particular relevance to microsatellite stable (MSS) colon cancer that responds poorly to immune checkpoint inhibitors (*97*). The MSS cell lines COLO205 and CACO2 showed both antineoplastic effects and transcriptional enrichment of calcium signaling following DAC and TAZ combination treatment (Fig. 3A and fig. S6A). Future studies will consider whether the DAC and TAZ combination helps overcome immunotherapy resistance in MSS colon cancers.

Rational EZH2i selection

We were surprised to find that the two most potent EZH2is (TAZ and CPI-1205) were the least toxic of all EZH2is tested in this study. The disconnect between cell viability and potency for the other toxic EZH2is suggests that these molecules have off-target activities. Recent studies have called for reevaluating the off-target effects of small molecules used experimentally and in clinical trials (including the EZH2i UNC1999 used in this study), suggesting that the mechanism of action behind their efficacy and/or toxicity may stem from different interactions than predicted (*98*, *99*).

Compounds such as TAZ and CPI-1205 that showed characteristics of low toxicity coupled with high potency also synergized the best with DAC. The limited single-agent toxicity of select EZH2is may be key for maximizing combination effects with DNMTis that require DNA synthesis for drug action. Given the broad interest in EZH2 inhibition in both laboratory and clinical settings (*46*, *47*), this study provides valuable insight as to how to rationally evaluate and assay these small molecules, including factors outside of cytotoxicity.

Relationship between epigenetic and transcriptional responses

The concept of an epigenetic switch in which the loss of one repressive mark induces compensation by a different silencing mechanism is not new to this field (*29*, *30*, *100*, *101*). In this study, we determined that an epigenetic switch between DNA methylation and H3K27me3 does not occur on a global scale but rather at specific Polycomb regulatory regions of the genome such as bivalent enhancers. Our study revealed a common theme for where the epigenetic switch occurs in which loss of DNA methylation at genomic regions with low basal levels of H3K27me3 induced increases in the repressive mark due to preexisting EZH2 occupancy. Notably, this reversion to PRC2-mediated repression following the removal of DNA methylation has been observed in normal developmental contexts where H3K27me3 helps maintain transposon repression after genome-wide induction of DNA methylation loss in mouse embryonic stem cells (*102*), adding evidence for the targetability of the interconversion of these two distinct silencing marks. Our combination treatment effectively blocked the epigenetic switch that occurs with single-agent DAC treatment, leading to accessibility of calcium signaling–associated transcription factor binding motifs (AP-1 and NFAT) for downstream regulation of transcriptional responses.

Early genome-wide studies reported anticorrelations between DNA methylation and H3K27me3 distributions leading to the paradigm that these marks are mutually exclusive (*29*, *101*). However, we and others report that these marks can indeed coexist and silence gene transcription in a cooperative manner (*39*, *67*, *68*). In this study, we identified over 300 PC genes (including TSGs such as *SFRP1*) that were dually silenced by both DNA methylation and H3K27me3 at promoter regions in HCT116 cells. Single-agent treatment with low-dose DAC or TAZ did not reactivate expression of these genes. Rather, the combination of DNMT and EZH2 inhibition was required to effectively remove both DNA methylation and H3K27me3, respectively, to permit expression of these genes. Our results are consistent with the observation that cancer cells are prone to coexistence of these modifications and that DNMTi and EZH2i combination treatment can effectively target genes that are dually modified for activation.

MATERIALS AND METHODS

Cell and tumoroid culture

Cell lines used in this study were from American Type Culture Collection (ATCC) (HTB-37, HTB-47, CCL-222, CCL-225, CCL-227, CCL-247, CRL-1932, CRL-1933, CRL-5803, and CRM-CCL-185) and maintained in ATCC-recommended culture medium, including McCoy's (Gibco, 16600-082), RPMI 1640 (Gibco, 11875-093), Leibovitz's L-15 (ATCC, 30-2008), or EMEM (ATCC, 30-2003) and A549 in RPMI 1640, all supplemented with 10 to 20% fetal bovine serum (MilliporeSigma, F0926) and 1% penicillin/streptomycin (Life Technologies, 15140-122) at 5% CO_2 and 37°C.

Tumoroids were derived from an $APC^{Min/+}$ mouse small intestine adenoma. After euthanasia with CO_2, the small intestine was excised, opened longitudinally, and vigorously washed 3× in phosphate-buffered saline (PBS). Adenomas were excised, minced, suspended in PBS, and centrifuged at 300*g* for 5 min. Pellets were resuspended in Dispase (STEMCELL Technologies, 07923) and incubated at 37°C for 10 min. Dissociated tissue was centrifuged again at 300*g* for 5 min, washed in Dulbecco's modified Eagle's medium (DMEM) (Life Technologies, 11965092), passed through a 70-μm filter, and centrifuged again. Dissociated cells were washed once more with DMEM, centrifuged, and resuspended in a 50:50 mixture of Matrigel (Corning, 356231):modified organoid HITES medium. Modified organoid HITES medium comprises DMEM/F12 50/50 (Life Technologies, 11330032) supplemented with 1× GlutaMAX (Gibco, 35050061), 1% penicillin/streptomycin (Life Technologies, 15140-122), insulin-transferrin-selenium mix (Gibco Invitrogen, 41400-045), 10% fetal bovine serum (MilliporeSigma, F0926) with hydrocortisone (1.6 ng/ml; Sigma-Aldrich, H0888), and murine epidermal growth factor (50 ng/ml; Thermo Fisher Scientific, PMG8041) added immediately before use. A total of 40 μl of this mixture was seeded into each well of a prewarmed 48-well plate, incubated for 10 min at 37°C to polymerize the Matrigel, and then covered with modified HITES medium. Once tumoroids formed, they were split using cold medium and gentle trituration and then replated within 50:50 Matrigel:modified HITES covered by modified HITES medium every 7 to 10 days.

Small interfering RNA transfection

ON-TARGETplus small interfering RNA (siRNA) SMARTpools (5 μl of 20 μM stock) targeting DNMT1, EZH1, EZH2, NFAT1, or Suppressor Of Zeste 12 (SUZ12) (Dharmacon, L-004605-00-0005, L-004217-00-0005, L-004218-00-0005, L-003606-00-0005, and L-006957-00-0010) and nontargeting control siRNA pools (Dharmacon, D-001810-10-05) were mixed with Lipofectamine RNAiMAX (5 μl;

Thermo Fisher Scientific, 13778075) in a total of 200 μl Opti-MEM (Life Technologies, 31985-062) and incubated for 20 min. McCoy's medium, with or without DAC and supplemented with 10% fetal bovine serum but no antibiotics, was refreshed, and the siRNA/lipid mix was added dropwise for a final siRNA concentration of 50 nM. Cells were collected 48 hours (siNFAT1) or 72 hours (other siRNA) after transfection.

Drug treatments

TAZ (Selleck Chemicals, S7128, and Cayman Chemical, 16174), CPI-1205 (Selleck Chemicals, S8353), EPZ0011989 (Selleck Chemicals, S7805), EPZ005687 (Cayman Chemical, 13966), GSK126 (Selleck Chemicals, S7061, and Cayman Chemical, 15415), GSK343 (Selleck Chemicals, S7164), GSK503 (Cayman Chemical, 18531), UNC1999 (Caymen Chemical, 14621), GSK3484862 (Chemietek, CT-CSKMI-714), CsA (Selleck Chemicals, S2286), LCK inhibitor (Cayman Chemical, 15135), and ionomycin (Cayman Chemical, 11932) were dissolved in dimethyl sulfoxide (DMSO) and stored at −20°C. DAC (Sigma-Aldrich, A3656) was dissolved in DMSO:PBS at a ratio of 1:150 and stored at −80°C. Each drug or the percentage of vehicle equivalent was applied to attached cells or to tumoroids suspended in 50:50 Matrigel:modified HITES medium.

Proliferation assays

To measure cell viability, cells were plated in 96-well plates at a density of 4000 to 5000 or 500 to 700 cells per well (for a 3- or 7-day exposure to drugs, respectively), treated the following day, and assayed with either CellTiter-Glo (Promega, G7570) or CellTiter-Fluor (Promega, G6080) kits according to the manufacturer's protocol. Measurements were taken using the Biottek Synergy Neo Microplate Reader. Background signal from medium-only wells was subtracted to obtain the final reported relative luminescence units (RLU; CellTiter-Glo) or relative fluorescence units (RFU; CellTiter-Fluor). IC_{50} values were generated using GraphPad Prism (RRID:SCR_002798).

To measure outgrowth of colon cancer cells after prolonged treatments, cells were plated in a six-well dish, and drug was applied to adhered cells the following morning. After 72 hours, cells were collected and replated directly in fresh medium and drugs for another 72 hours, for a total of 3 to 6 days of "pretreatment" depending on the cell line. Following pretreatment, cells were plated into either 12-well (10,000 to 20,000 cells per well) or 96-well (500 to 700 cells per well) dishes and treated for a final time, which is represented as "day 0" following pretreatments on confluency graphs. From these samples, 9 to 12 images were captured for each well at each time point and the percentage of confluency calculated using a Sartorius IncuCyte S3.

For prolonged treatment of tumoroids, media and drugs were refreshed every 3 to 4 days and tumoroids split in a 1:4 ratio (regardless of response to drug treatment) every 7 to 10 days. At 21 days, bright-field images from three wells per treatment were taken using the 4× objective of a Nikon Eclipse TS2R microscope. Tumoroids were categorized and counted on the basis of morphology categories, and the counter was blinded to the treatment.

SFRP1-NLuc reporter assay

The *SFRP1*-NLuc reporter cell line was created using CRISPR-Cas9 to insert an NLuc cassette into exon 2 of an endogenous *SFRP1* allele. To measure NLuc activity in *SFRP1*-NLuc experiments, the CellTiter-Fluor assay was duplexed with the Nano-Glo Luciferase Assay System (Promega, N1110). For these experiments, cells were plated in 96-well plates as above for the cell viability assays, and media and drugs were refreshed after 72 hours for the 6-day synergy measurements. To duplex the assays, CellTiter-Fluor was used at a 5× concentration preceding the Nano-Glo assay. NanoGlo reagent was applied according to the manufacturer's protocol, and a Synergy Neo Microplate Reader was used to obtain RLU. After background subtraction from medium-only wells, RLU were normalized to CellTiter-Fluor RFU to account for cell viability. This normalization was also used as the input for the synergy score calculations. The expected drug combination responses were calculated on the basis of the Bliss independence model using SynergyFinder2.0 (*51*). These scores are the average excess response due to the drug interaction, and a score greater than 10 is considered likely synergistic (https://synergyfinder.fimm.fi/synergy/synfin_docs/#datanal). Deviations between observed and expected responses with positive and negative values denote synergy and antagonism, respectively.

Immunofluorescence staining

HCT116 cells were grown on Lab-Tek chamber slides (Thermo Fisher Scientific, 154534) and treated for 72 hours with CsA preceding a 1-hour ionomycin challenge. Slides were rinsed in PBS, fixed with 4% paraformaldehyde for 15 min, and rinsed again with PBS. Paraformaldehyde was neutralized, and cells were permeabilized with permeabilization buffer (PBS, 0.3% Triton X-100, and 200 mM glycine) for 20 min. Cells were incubated with blocking buffer [PBS, 2% bovine serum albumin (BSA), 0.1% Triton X-100, and 10% goat serum] for 30 min, followed by incubation with primary antibody against NFAT1 [1:100; Cell Signaling Technology, 5861, RRID:AB_10834808; which was validated by Western blot of HCT116 lysates with siRNA-mediated NFAT1 knockdown (fig. S7B)] in antibody buffer (PBS, 0.1% BSA, and 0.1% Triton X-100) for 60 min. Cells were washed twice with antibody buffer, incubated with secondary antibody (1:200; Thermo Fisher Scientific, A-11034, RRID:AB_2576217) for 30 min, and washed twice with antibody buffer. Slides were coverslipped with SlowFade Gold mounting medium (Thermo Fisher Scientific, S36936) and imaged using the 40× objective of an Olympus BX51 microscope and the assistance of the VAI Optical Imaging Core (RRID:SCR_021968).

Flow cytometry

Cells treated with 5 μM CsA for 72 hours were collected by trypsinization and centrifuged at 300*g* for 10 min. Cell pellets were resuspended in 0.5 ml of cold PBS, and 4.5 ml of cold 70% ethanol was added dropwise to cells while gently vortexing. Cells were fixed on ice for 2 hours, centrifuged at 500*g* for 10 min, washed in PBS, and centrifuged again. Cell pellets were resuspended in 500 μl of propidium iodide staining solution [500 μl PBS, ribonuclease A (RNase A) (100 μg/ml), and propidium iodide (50 μg/ml)] and incubated at 4°C for 2 hours. Flow cytometry and analysis were performed by the VAI Flow Cytometry Core (RRID:SCR_022685) using a CytoFLEX S Flow cytometer.

Western blotting

Cells were lysed on ice in cold CSK lysis buffer [10 mM Pipes (pH 7.0), 300 mM sucrose, 100 mM NaCl, 3 mM $MgCl_2$, 0.1% Triton X-100, universal nuclease, and protease inhibitor cocktail (Roche cOmplete Mini tablets, EDTA-free)] for 30 min and then centrifuged for 10 min at 10,000*g* to remove insoluble protein. Total protein in the supernatant was quantified by Bradford assay (Bio-Rad 5000006), denatured in SDS loading buffer, and boiled for 10 min. Two to 5 μg of protein was size-separated by SDS–polyacrylamide gel electrophoresis and transferred to a polyvinylidene difluoride membrane. Membranes were blocked for one hour at room temperature (PBS, 0.1% Tween 20, and 5% BSA), washed in PBST (PBS and 0.1% Tween 20), and incubated with primary antibodies against β-actin (1:1000; Cell Signaling Technology, 4970, RRID:AB_2223172), EZH1 (1:1000; Cell Signaling Technology, 42088, RRID:AB_2799212), EZH2 (1:1000; Cell Signaling Technology, 5246, RRID:AB_10694683), H3 (1:50,000; EpiCypher, 13-0001). H3K27me3 (1:2000; Cell Signaling Technology, 9733, RRID:AB_2616029), NFAT1 (1:1500; Cell Signaling Technology, 5861, RRID:AB_10834808), and SUZ12 (1:1000; Abcam, ab12073, RRID:AB_442939) in blocking buffer overnight at 4°C. The H3K27me3 antibody was chosen for its high specificity and selectivity among H3K27me3 antibodies profiled by our laboratory on histone peptide arrays (*103*). Membranes were washed in PBST and incubated in horseradish peroxidase–conjugated secondary antibody (1:10,000; Sigma-Aldrich, GENA934, RRID:AB_2722659) for 1 hour at room temperature. Membranes were washed again in PBST, incubated in enhanced chemiluminesence, and imaged with film. ImageJ (RRID:SCR_003070) densitometry was used to quantify band intensity.

High-resolution melt assay for DNA methylation

DNA was isolated from treated cell pellets using a DNeasy Blood & Tissue Kit (QIAGEN, 69504) according to the manufacturer's protocol. The EZ DNA Methylation Kit (Zymo, D5002) was used to bisulfite-convert 500 ng of DNA per sample according to the manufacturer's protocol. Bisulfite-converted DNA was eluted in 10 μl of M-elution buffer from the kit and brought up to 54 μl total with deoxyribonuclease (DNase)–free water. Five microliters of the bisulfite converted DNA was combined with 10 μl of Precision Melt Supermix for high-resolution melt analysis (Bio-Rad, 1725112) and 2 μl of forward and reverse primers (2 μM stock) and brought to 20 μl with DNase-free water. A Bio-Rad CFX Opus93 real-time PCR system was used to amplify the DNA at a 60°C annealing temperature for 39 cycles and then perform a melt analysis from 65° to 95°C with 0.1°C/10-s increments. The melting temperature (T_m) at the maximum reported RFU value was reported for each amplicon. An amplicon from an unmethylated gene, *RPL30*, was used to control for bisulfite conversion (forward, 5′-TAATTTAGAAGAGATAGAG AATAGGATAGGAATTTTAG-3′; reverse, 5′-ACCATCTTAACGA CTACTATTAATAAATAAACTCCTAC-3′ primers; seven CpGs covered). Amplicons in the hypermethylated CGI promoter of *SFRP1* (forward, 5′-AGGGGTATTTAGTTGTTGGTTTGTTG-3′; reverse, 5′-CTTCTACACCAAACCACCTCAATA-3′ primers; seven CpGs covered) or a methylated chromosome 6 pericentromeric (*Chr6PCH*) locus (forward, 5′-GGGTTATTTCGTAGGAGGGAG GTTGTTATAGTTTTG-3′; reverse, 5′-CCTCAATACGCCATTCT CTACTCCCCAAAACC-3′ primers; six CpGs covered) were used to report on DNA methylation changes.

RNA isolation, cDNA synthesis, and qRT-PCR

TRIzol reagent (Invitrogen, 15596026) was added directly to adhered cells, collected, and stored at −80°C. After thawing, total RNA was extracted following the manufacturer's protocol, and RNA was resuspended in diethyl pyrocarbonate nuclease-free water. The High-Capacity cDNA Reverse Transcription Kit (Applied Biosystems, 4368814) with the addition of RNase was used according to the manufacturer's protocol to synthesize cDNA from 2 μg of RNA. Using the KAPA SYBR FAST qPCR Kit (Roche, 07959567001) according to the manufacturer's protocol and run on the Bio-Rad CFX Opus93 Real-Time PCR System, qRT-PCR was performed on biological duplicates or triplicates (noted in figure legends) for each experiment and technical duplicates for each gene (Table 1) and sample from the biological replicates. Data were analyzed using $2^{-\Delta\Delta(\mathrm{Ct})}$ method (*104*) where the fold change was determined by normalizing to the *RPL4* housekeeping gene and an untreated or vehicle-treated sample.

Chromatin immunoprecipitation

Cells exposed to drugs for 72 hours were fixed in buffer [1% formaldehyde, 50 mM Hepes-KOH (pH 7.6), 100 mM NaCl, 1 mM EDTA (pH 8.0), and 0.5 mM EGTA (pH 8.0)] for 10 min at room temperature with shaking and then quenched with 125 mM glycine for 5 min at room temperature. Cells were scraped into cold PBS, washed 2× with cold PBS, flash-frozen in liquid N_2, and stored at −80°C until use. Thawed pellets were lysed in LB1 [50 mM Hepes-KOH (pH 7.6), 140 mM NaCl, 1 mM EDTA, 10% glycerol, 0.5% NP-40, 0.25% Triton X-100, and Roche protease inhibitor cocktail] for 20 min with rotation at 4°C and cleared by centrifugation at 300*g* for 5 min at 4°C. Supernatant with intact nuclei was set aside. Cell pellets were lysed again in 4× LB1 (LB1 with 2% NP-40 and 1% Triton X-100) for 20 min. Intact nuclei from this and the saved supernatant were collected by centrifugation at 1700*g* for 5 min at 4°C, resuspended and washed in LB2 [10 mM tris-HCl (pH 8.0), 1 mM EDTA, 0.5 mM EGTA, 200 mM NaCl, and protease cocktail inhibitor] for 10 min with rotation at 4°C, and collected again by centrifugation at 1700*g* for 5 min at 4°C. Nuclei were gently rinsed 2× with LB3 [10 mM tris-HCl (pH 8.0), 1 mM EDTA, 0.5 mM EGTA, 0.01% NP-40, and protease cocktail inhibitor] without disturbing the pellet. Nuclei were resuspended in 1 ml of LB3 and transferred to a 1-ml milliTUBE (Covaris). Chromatin was sheared to a range of 300– to 600–base pair (bp) fragments using a Covaris E220 evolution focused ultrasonicator with the following parameters: peak power (140.0), duty factor (5.0), cycles/burst (200), duration (600 s), and temperature (4°C). Sheared chromatin was quantified by Bradford assay, 450 μg of chromatin was brought to 500 μl in LB3, and 500 μl of ChIP cocktail mix [40 mM tris-HCl (pH 7.6), 150 mM NaCl, 1 mM EDTA (pH 8.0), 1% Triton X-100, 0.5% NP-40, and protease inhibitor cocktail] was added. Prepared chromatin was precleared by incubation with 20 μl of prewashed Dynabeads Protein G magnetic beads (Invitrogen, 10004D) for 3 hours at 4°C with rotation. After bead removal, 10% input (100 μl) of precleared chromatin was removed and set aside. Precleared chromatin was immunoprecipitated with 5 μl of H3K27me3 antibody (Cell Signaling Technology, 9733, RRID:AB_2616029) overnight at 4°C with constant rotation. Protein G magnetic beads [35 μl per immunoprecipitation (IP)] were blocked in buffer containing PBS, 0.5% BSA, and 20 μg Herring sperm DNA (Sigma-Aldrich, D7290) with rotation at 4°C overnight. Blocked beads were washed 3× with PBS and 0.5% BSA and 2× with WB1 [50 mM tris-HCl (pH 7.6), 150 mM NaCl, 5 mM EDTA (pH 8.0), 0.5% NP-40, and 1% Triton X-100]. Immunochromatin complexes were incubated with blocked beads for 3 hours with rotation at 4°C. Bead-immunochromatin complexes were then washed 3× for 5 min with rotation at 4°C with WB1, 3× with WB2 [50 mM tris-HCl

Table 1. qRT-PCR genes and primers.

Gene	Forward (5′-3′)	Reverse (5′-3′)
ATP2B2	AAGAACATCCTGGGCCATGC	TGGAACATCTTCTCGCCAACA
CACNA1C	TCAACAACGCCAACAACACC	GGCACCTGTTGGAGCTGAG
ELMO1	TGAGACCTGCAACGACTTCC	TCACCACCTGCATTACCTTGT
FOS	TGACTGATACACTCCAAGCGG	GGCAATCTCGGTCTGCAAAG
GCNT2	TGACATGGAAGACAGACACGG	TCCACAGTAAGGGGGTAGGT
GRHL3	CTGAAGGGGCTGAGGAATGC	GACGTGGTTGCTGTAATGCTG
IFI27	TCTGGCTCTGCCGTAGTTTT	GAACTTGGTCAATCCGGAGA
JUN	GTCCGAGAGCGGACCTTATG	GGTGAGGAGGTCCGAGTTCT
KRT17	AAGGATGCCGAGGATTGGTT	ACTGCAGCTCTATCTCCAAGG
LAT	CGAGCTACGAGAACGAGGAA	GCCTGGGTTGTGATAGTCGT
LCK	AACAAACTCCTGGACATGGCA	GCCCGAAGGTCACGATGAATA
NFATC1	AAAACTGACCGGGACCTGTG	GAACGGGGCTGGTTATCCTC
NFATC2	AGAATGCCACGAGCCAAAGA	AGCTAAGGTGTGTGTCTATCAGC
NOS1	CTCCTGGCTCAACCGGATAC	TGCCAGAAGCTTCGGAAAGG
RPL4	ATCCAAAGAGCCCTTCGAGC	CTGGCGAAGAATGGTGTTCC
SFRP1	CATGCAGTTCTTCGGCTTCT	GATTTCAACTCGTTGTCACAGG
TMEM35A	GCTCAGCAAGGATGCCTACA	GGCACCAATGCTTTTTCGGA

(pH 7.6), 500 mM NaCl, 5 mM EDTA (pH 8.0), 0.5% NP-40, and 1% Triton X-100], 2× with WB1, and 1× with low-salt TE [10 mM tris-HCl (pH 8.0), 1 mM EDTA (pH 8.0), and 50 mM NaCl]. Beads were incubated in 50 μl of elution buffer [10 mM tris-HCl (pH 8.0), 10 mM EDTA, 150 mM NaCl, 5 mM dithiothreitol, and 1% SDS] at 65°C for 15 min in 50-μl volume to elute immunochromatin complexes. The elution step was repeated, and eluates were combined. Eluents and input were incubated overnight at 65°C with constant shaking to reverse cross-links, followed by incubation at 37°C for 1 hour with DNase-free RNase A and then at 37°C for 2 hours with 10 μl of Proteinase K (20 mg/ml of stock). DNA was isolated with a 1.5× ratio of KAPA Pure Beads (KAPA Biosystems, KK8000) to DNA volume.

siQ-ChIP library preparation and sequencing

Immunoprecipitated fragments and saved inputs were quantified with the Qubit dsDNA High Sensitivity Assay kit (Invitrogen, Q32851), and 10 ng of purified DNA for each IP and input sample were used for library preparation with the KAPA Hyper Prep Kit (Kapa Biosystems, KR0961). TAZ and combo treatments required two IPs per biological replicate to attain enough material for library preparation, and this doubling has been accounted for in the parameters for siQ-ChIP (*59*, *60*) for these samples. Library preparation including fragment end-repair, A-tail extension, and adapter ligation was conducted per the manufacturer's instructions (KAPA Biosystems). Adapter-ligated fragments were amplified with 11 cycles following the recommended thermocycler program, and DNA was purified with two rounds of purification using KAPA Pure Beads (KK8000). Quality and quantity of the finished libraries were assessed using a combination of the Agilent DNA High Sensitivity chip (Agilent Technologies Inc.), the QuantiFluor dsDNA System (Promega Corp., Madison, WI, USA), and the Kapa Illumina Library Quantification qPCR assays (KAPA Biosystems). Individually indexed libraries were pooled and 75-bp, paired-end sequencing was performed on an Illumina NextSeq 500 sequencer using a 150-bp HO sequencing kit (v2) (Illumina Inc., San Diego, CA, USA), or 50-bp, paired-end sequencing was performed on an Illumina NovaSeq6000 sequencer using an S2, 100-bp sequencing kit to a minimum read depth of 50 M read pairs per IP library and 100 M read pairs per input library. Base calling was done by Illumina RTA3, and output of NextSeq Control Software (NCS) was demultiplexed and converted to FastQ format with Illumina Bcl2fastq (v1.9.0).

siQ-ChIP-seq processing and analysis

siQ-ChIP sequencing reads were 3′ trimmed and filtered for quality and adapter content using TrimGalore (v0.5.0), and quality was assessed by FastQC (v0.11.8). Reads were aligned to human assembly hg38 with bowtie2 (v2.3.5, RRID:SCR_016368) and were deduplicated using removeDups from samblaster (v.0.1.24) (*105*). Aligned BAM files were used for quality control analysis with deepTools (v3.2.0) "plotFingerprint" and "plotPCA" functions. Aligned SAM files were then processed for paired-end reads with high mapping quality (MAQ ≥ 20), correct pair orientation (Sam Flags = 99, 163), and fragment length as described for siQ-ChIP (https://github.com/BradleyDickson/siQ-ChIP). Param.in files were prepared for each sample with all required parameters and measurements required for siQ-ChIP normalization. IP tracks (with H3K27me3 efficiency values) and comparative responses between drug treatments (relative to vehicle) were generated with execution of getsiq.sh (v: February 2021) with the EXPlayout file [note: params.in and EXPlayout file are provided with the Gene Expression Omnibus (GEO) accession]. Each individual inhibitor-treated biological replicate was compared to each individual vehicle-treated biological replicate.

To determine the change in H3K27me3 distributions between inhibitor-treated samples and vehicle-treated samples, each inhibitor-treated biological replicate (e.g., DAC301) was individually compared to the two vehicle-treated biological replicates (e.g., DAC301vsVeh1 and DAC301vsVeh2), and the average $\log_2$ fold change in response (area of peak in inhibitor treatment/area of peak in vehicle treatment) was calculated. Next, conserved peaks between inhibitor-treated biological duplicates were determined by calculating the proximity of replicate 1 peaks to replicate 2 peaks (e.g., DAC301 and DAC302) using the "closest" command from bedtools (v2.25.0). Peaks were considered conserved among biological replicates if the peaks overlapped or were within 200 bp of each other. Last, the average $\log_2$ fold change in response was calculated for the peaks conserved between the two inhibitor-treated biological replicates. Peaks were considered significant if the $\log_2$ fold change in response was ≥ 1.0 (increase in H3K27me3) or ≤ -1.0 (decrease in H3K27me3).

ChromHMM (v1.23)

Custom ChromHMM (*106*) annotations for the HCT116 cell line were built with publicly available datasets (Table 2). For the H3K27me3 ChIP-seq dataset, we used our vehicle-treated HCT116 H3K27me3 ChIP-seq data generated in this study. The original raw fastq.gz files were downloaded, reprocessed, and aligned using the workflow described under siQ-ChIP processing and analysis. All aligned BAM files were binarized using "BinarizeBam" and then fed into "LearnModel" to build a 15-state chromatin model. Chromatin states were assigned manually by considering the enrichment emissions for histone PTMs (fig. S4H), coverage of the genome (fig. S4I), and proximity to TSSs. Enrichment overlap analysis with siQ-ChIP peaks, Repli-Seq phases, and differently expressed genes was conducted with the "OverlapEnrichment" function using the genomic coordinates for each dataset.

Repli-Seq data accession and analysis

Sixteen-phase Repli-Seq data (measuring replication timing from early to late replication) were downloaded (GEO: GSE137764) (*63*), and each phase of replication timing was separated into their own genomic coordinates (both bed and bigwig files) for use in integrative ChromHMM, siQ-ChIP-seq, and gene expression analysis.

EM-seq library preparation and sequencing

Libraries were prepared by the Van Andel Institute Genomics Core (RRID:SCR_022913) from an input of 41 to 51 ng of ChIP DNA (taken directly from DNA immunoprecipitated for siQ-ChIP-seq) using the NEBNext EM-seq Kit (New England Biolabs, E7120L). The denaturation method used was 0.1 N of sodium hydroxide, according to the protocol, and 8 cycles of PCR amplification were performed. Quality and quantity of the finished libraries were assessed using a combination of the Agilent High Sensitivity DNA chip (Agilent Technologies Inc., 5067-4626) and QuantiFluor dsDNA System (Promega, E2670). Paired-end sequencing (150 bp) was performed on an Illumina NovaSeq6000 sequencer using an S4, 300-bp sequencing kit (Illumina Inc., San Diego, CA, USA), with 10% PhiX to a minimum read depth of 100 M read pairs per library. Base calling was done by Illumina RTA3, and output of NCS was demultiplexed and converted to FastQ format with Illumina Bcl2fastq (v1.9.0).

EM-seq processing and analysis

EM-seq reads were aligned to human genome build hg38, duplicate-marked (samblaster, RRID:SCR_000468), and sorted (samtools, RRID:SCR_002105) using the "biscuitBlaster" pipeline from BISCUIT (v0.3.16) (https://huishenlab.github.io/biscuit/). Cytosine retention and callable single-nucleotide polymorphism mutations were computed with "biscuit pileup" and output into a VCF file. Cytosine β values and coverage were extracted with "biscuit vcf2bed" and CpG methylation status was merged with "biscuit mergecg."

Quality control of the ChIP-EM-seq dataset was assessed several ways. First, principal components analysis ["plotPCA" deepTools (v3.2.0)] of both the siQ-ChIP and EM-seq libraries demonstrated that samples clustered based on their drug treatment (fig. S4D). To determine that EM-seq libraries truly were enriched for H3K27me3 fragments, k-means clustering from deepTools ($n = 4$ clusters) was conducted to stratify PC genes around the TSS by the efficiency of H3K27me3 IP (fig. S4E, top). Next, we calculated the average CpG read coverage in the EM-seq libraries for each of the H3K27me3 clusters and showed that the clusters with the highest H3K27me3 level (C1 and C2) also have the highest average read coverage, indicating that our approach effectively enriched for H3K27me3 in a quantitative manner and was sufficiently covered by EM-seq to interrogate DNA methylation levels (fig. S4E, bottom). CpH dinucleotides (control for EM conversion) showed less than 0.5% cytosine methylation indicating that we achieved >99% conversion efficiency on all EM-seq libraries (fig. S4F).

To assess the direct relationship between H3K27me3 and DNA methylation levels, we divided the genome into 100-bp bins, calculated the average H3K27me3 efficiency between biological replicates for each 100 bp bin, calculated z scores for each bin considering the H3K27me3 efficiency across all bins in the vehicle-treated samples, and lastly subdivided the bins based on z score into different H3K27me3 categories (fig. S4G). CpG coordinates were intersected with the 100-bp H3K27me3 bin coordinates using "intersect" from bedtools (RRID:SCR_006646) (*107*) and

Table 2. ENCODE and GEO accession numbers for public ChIP-seq datasets used.

Histone PTM	ENCODE accession (*120*)	GEO accession
H3K4me1	ENCSR161MXP	GSE95958
H3K4me3	ENCSR333OPW	GSE96123
H3K9me3	N/A (Rothbart laboratory generated)	GSM4668119, GSM4668118
H3K27ac	ENCSR661KMA	GSE96299
H3K36me3	ENCSR091QXP	GSE95914

calculated the average β value of the CpGs contained within each 100-bp H3K27me3 bin.

For integrative analysis with ChromHMM, siQ-ChIP, and gene expression, cytosine retention and coverage values were combined, and a CpG was retained for downstream analysis if it was covered by ≥8 sequencing reads. Bed files were constructed for each sample with the calculated β value for each CpG and converted to bigwigs using UCSC Browser Tools (v: March 2017).

Integrative genomic analysis

As described in the respective sections above, bigwig files were generated for each sample for genome-wide H3K27me3 efficiency (siQ-ChIP-seq) and DNA methylation β values (EM-seq). Bed files with genomic coordinates for differential H3K27me3 peak analysis, ChromHMM chromatin–state annotations, and Repli-Seq phases were generated as described above. Integrated siQ-ChIP-seq and EM-seq analysis was conducted with deepTools (v3.2.0) (*108*) by constructing matrices with "computeMatrix" across queried genomic coordinates with the respective bigwig data and visualizing the summarized integration with "plotProfile" and "plotHeatmap."

Bivalent enhancers that demonstrated an increase in H3K27me3 efficiency following DAC treatment were identified by intersecting the peak coordinates with the ChromHMM EnhBiv coordinates using "intersect" from bedtools (*107*). Motif enrichment analysis was conducted on the intersected bivalent enhancer coordinates (∓10 kb) using "findMotifsGenome.pl -len 8,10,12" from HOMER (v4.11.1) (*109*).

Genomic DNA isolation

Genomic DNA was extracted using the DNeasy Blood & Tissue Kit (QIAGEN, 69504) following the standard protocol. Samples were then treated with RNase A (1 mg/ml) at 37°C for 30 min. DNA was reprecipitated with $^{1}/_{10}$ volume of 3 M sodium acetate (pH 4.8) and 2.5 volumes of 100% ethanol and stored overnight at −20°C. Precipitated DNA was pelleted by centrifugation at 17,090*g* for 30 min at 4°C. The pelleted DNA was washed twice with 70% ethanol, allowed to dry for 15 min, and resuspended in nuclease-free water.

Infinium MethylationEPIC BeadChip (EPIC array)

Genomic DNA was quantified with the Qubit dsDNA High Sensitivity Assay kit (Invitrogen, Q32851), and 1.5 μg of genomic DNA was submitted to the VAI Genomics Core (RRID:SCR_022913) for quality control analysis, bisulfite conversion, and DNA methylation quantification using the Infinium MethylationEPIC BeadChIP (Illumina) processed on an Illumina iScan system following the manufacturer's standard protocol (*110*, *111*).

EPIC array data processing and analysis

All analyses were conducted in the R statistical software (v4.1.2) (R Core Team). Raw IDAT files for each sample were processed using the Bioconductor (RRID:SCR_006442) package SeSAMe (v1.8.12) for extraction of probe signal intensity values, normalization of probe signal intensity values, and calculation of β values from the normalized probe signal intensity values (*112*–*114*). The β value is the measure of DNA methylation for each individual CpG probe, where a minimum value of 0 indicates a fully unmethylated CpG and a maximum value of 1 indicates a fully methylated CpG in the population. CpG probes with a detection $P > 0.05$ in any one sample were excluded from the analysis. DMRs were called using the Bioconductor package DMRcate (v3.13), and regions were considered differentially methylated if at least five contiguous CpGs demonstrated a mean difference of 0.15 methylation change in the drug-treated cells compared to vehicle-treated HCT116 cells.

Construction and sequencing of directional total RNA-seq libraries

Libraries were prepared by the Van Andel Institute Genomics Core (RRID:SCR_022913) from 500 ng of total RNA using the KAPA RNA HyperPrep Kit (Kapa Biosystems, Wilmington, MA, USA). Ribosomal RNA material was reduced using the QIAseq FastSelect–rRNA HMR Kit (QIAGEN, Germantown, MD, USA). RNA was sheared to 300 to 400 bp. Before PCR amplification, cDNA fragments were ligated to IDT for Illumina TruSeq UD Indexed adapters (Illumina Inc., San Diego CA, USA). Quality and quantity of the finished libraries were assessed using a combination of the Agilent DNA High Sensitivity chip (Agilent Technologies Inc.) and QuantiFluor dsDNA System (Promega Corp., Madison, WI, USA). Individually indexed libraries were pooled and 50 bp, paired-end sequencing was performed on an Illumina NovaSeq6000 sequencer to an average depth of 50 M raw paired-reads per transcriptome. Base calling was done by Illumina RTA3, and output of NCS was demultiplexed and converted to FastQ format with Illumina Bcl2fastq (v1.9.0).

RNA-seq processing and analysis

Raw 50-bp paired-end reads were trimmed with TrimGalore! (www.bioinformatics.babraham.ac.uk/projects/trim_galore/) (RRID:SCR_011847), followed by quality control analysis with FastQC. Trimmed reads were aligned to GRCh38.p12 and indexed to GENCODE v29 via STAR (v2.5.3a) aligner with flags "-twopassMode Basic\ -quantMode GeneCounts" for feature counting.

ReadsPerGene output count files were constructed into a raw read count matrix in R. Low-count genes were filtered (one count in at least one sample) before edgeR (v3.36.0) count normalization and differential expression analysis with "voomWithQualityWeights" and quasi-likelihood fit set to robust. Principal components analysis was calculated using "prcomp" in the R stats package on the normalized expression matrix. Differential expression analysis was conducted with "voomWithQualityWeights" and a quasi-likelihood fit set to robust. Each dataset was treated separately for differential expression analysis (i.e., day 3 acute treatment, day 6 prolonged treatment, and CsA treatments), and all inhibitor treatments were compared to their respective vehicle samples. Genes were considered differentially expressed if $|\log_2 FC| \geq 1$ and false discovery rate (FDR) ≤ 0.01. Venn diagrams of overlapping genes were generated using BioVenn (*115*).

TE analysis

TE analysis of total RNA-seq datasets was conducted with SQuIRE (v0.9.9.92) (https://github.com/wyang17/SQuIRE) (*116*). TEs were aligned to hg38, counted, and analyzed for differential expression relative to the vehicle-treated samples using "Map," "Count," and "Call" commands, respectively. TEs were considered differentially expressed if $|\log_2 FC| \geq 1$ and adjusted $P \leq 0.01$.

Gene set enrichment analysis

GSEA (v4.1.0) (*117*) was conducted across the following curated gene set databases: HALLMARK, c2.cgp, c2.cp.biocarta, c2.cp.kegg, c2.cp.reactome, and c3.tft.v2023.1. Phenotype comparisons were set to combo versus REST for all analysis with weighted enrichment statistic and Signal2Noise settings for ranking genes. Maximum and minimum sizes of a gene set were set to 2500 and 15 genes, respectively. Genes marked as a "core enrichment" gene were used for heatmap row z score analysis of normalized counts per million (CPM) values.

TCGA analysis

"Gene Expression Quantification" data for "Transcriptome Profiling" of primary solid tumors were queried, downloaded, and prepared using the Bioconductor package TCGAbiolinks (*118*) for the following datasets: COAD/READ (*119*), BRCA (*77*), and OV (*78*). Prepared gene counts were normalized by library size and overall transcription level with the Bioconductor package edgeR. For each cancer dataset, the respective AIM derived from Li *et al.* (*76*) was used for supervised clustering (clustering_method = "average"; clustering_distance = "correlation") of the sample normalized gene counts using pheatmap. Samples were assigned into AIM high and low clusters based on the first column dendrogram branch. After AIM categories were assigned for each sample, supervised clustering of the core enrichment genes from the Kyoto Encyclopedia of Genes and Genomes (KEGG) calcium signaling gene set (identified from GSEA analysis of day 3 acute treatment combo versus REST) was done using pheatmap (v1.0.12). For direct comparison of the AIM and calcium signaling gene sets, the average z score across the respective gene set was calculated for each sample and used for Pearson correlation analysis.

PRC2 inhibition in vitro assay

Reactions (10 μl) containing 150 nM PRC2 [comprising EZH2, SUZ12, Embryonic Ectoderm Development (EED), and RbAp46/48; Active Motif, 31887], 1 μM recombinant nucleosomes wrapped with 187-bp DNA (EpiCypher, 16-2004), and 1 μCi of ^{3}H-SAM (PerkinElmer) in KMT reaction buffer [50 mM tris (pH 8.8), 2 mM $MgCl_2$, 0.02% Triton X-100, and 1 mM dithiothreitol] with indicated amounts of EZH2is or an equivalent concentration of DMSO were incubated for 1 hour at room temperature. Reactions were stopped by the addition of trifluoracetic acid to a final concentration of 0.5%, neutralized by diluting with 150 μl of 50 mM $NaHCO_3$, and transferred to streptavidin-coated FlashPlates (PerkinElmer). Plates were incubated for 15 min, sealed, and counted in a MicroBeta2 liquid scintillation counter (PerkinElmer MicroBeta2) for 1 min per sample. Percent activity was calculated by comparing to DMSO control, and IC_{50} values were calculated using GraphPad Prism (RRID:SCR_002798).

Supplementary Materials

This PDF file includes:

Figs. S1 to S9

REFERENCES AND NOTES

1. D. Hanahan, Hallmarks of cancer: New dimensions. *Cancer Discov.* **12**, 31–46 (2022).
2. S. B. Baylin, P. A. Jones, Epigenetic determinants of cancer. *Cold Spring Harb. Perspect. Biol.* **8**, (2016).
3. B. P. Berman, D. J. Weisenberger, J. F. Aman, T. Hinoue, Z. Ramjan, Y. Liu, H. Noushmehr, C. P. E. Lange, C. M. van Dijk, R. A. E. M. Tollenaar, D. Van Den Berg, P. W. Laird, Regions of focal DNA hypermethylation and long-range hypomethylation in colorectal cancer coincide with nuclear lamina–associated domains. *Nat. Genet.* **44**, 40–46 (2011).
4. H. Shen, P. W. Laird, Interplay between the cancer genome and epigenome. *Cell* **153**, 38–55 (2013).
5. K. E. Varley, J. Gertz, K. M. Bowling, S. L. Parker, T. E. Reddy, F. Pauli-Behn, M. K. Cross, B. A. Williams, J. A. Stamatoyannopoulos, G. E. Crawford, D. M. Absher, B. J. Wold, R. M. Myers, Dynamic DNA methylation across diverse human cell lines and tissues. *Genome Res.* **23**, 555–567 (2013).
6. K. B. Chiappinelli, P. L. Strissel, A. Desrichard, H. Li, C. Henke, B. Akman, A. Hein, N. S. Rote, L. M. Cope, A. Snyder, V. Makarov, S. Budhu, S. Buhu, D. J. Slamon, J. D. Wolchok, D. M. Pardoll, M. W. Beckmann, C. A. Zahnow, T. Merghoub, T. Mergoub, T. A. Chan, S. B. Baylin, R. Strick, Inhibiting DNA methylation causes an interferon response in cancer via dsRNA including endogenous retroviruses. *Cell* **162**, 974–986 (2015).
7. D. Roulois, H. Loo Yau, R. Singhania, Y. Wang, A. Danesh, S. Y. Shen, H. Han, G. Liang, P. A. Jones, T. J. Pugh, C. O'Brien, D. D. De Carvalho, DNA-demethylating agents target colorectal cancer cells by inducing viral mimicry by endogenous transcripts. *Cell* **162**, 961–973 (2015).
8. M. J. Topper, M. Vaz, K. A. Marrone, J. R. Brahmer, S. B. Baylin, The emerging role of epigenetic therapeutics in immuno-oncology. *Nat. Rev. Clin. Oncol.* **17**, 75–90 (2020).
9. H. E. Ghoneim, Y. Fan, A. Moustaki, H. A. Abdelsamed, P. Dash, P. Dogra, R. Carter, W. Awad, G. Neale, P. G. Thomas, B. Youngblood, De novo epigenetic programs inhibit PD-1 blockade-mediated T cell rejuvenation. *Cell* **170**, 142–157.e19 (2017).
10. D. Peng, I. Kryczek, N. Nagarsheth, L. Zhao, S. Wei, W. Wang, Y. Sun, E. Zhao, L. Vatan, W. Szeliga, J. Kotarski, R. Tarkowski, Y. Dou, K. Cho, S. Hensley-Alford, A. Munkarah, R. Liu, W. Zou, Epigenetic silencing of T_H1-type chemokines shapes tumour immunity and immunotherapy. *Nature* **527**, 249–253 (2015).
11. M. L. Stone, K. B. Chiappinelli, H. Li, L. M. Murphy, M. E. Travers, M. J. Topper, D. Mathios, M. Lim, I.-M. Shih, T.-L. Wang, C.-F. Hung, V. Bhargava, K. R. Wiehagen, G. S. Cowley, K. E. Bachman, R. Strick, P. L. Strissel, S. B. Baylin, C. A. Zahnow, Epigenetic therapy activates type I interferon signaling in murine ovarian cancer to reduce immunosuppression and tumor burden. *Proc. Natl. Acad. Sci. U S A* **114**, E10981–E10990 (2017).
12. R. L. Siegel, K. D. Miller, A. Goding Sauer, S. A. Fedewa, L. F. Butterly, J. C. Anderson, A. Cercek, R. A. Smith, A. Jemal, Colorectal cancer statistics, 2020. *CA Cancer J. Clin.* **70**, 145–164 (2020).
13. T. Hinoue, D. J. Weisenberger, C. P. E. Lange, H. Shen, H.-M. Byun, D. Van Den Berg, S. Malik, F. Pan, H. Noushmehr, C. M. van Dijk, R. A. E. M. Tollenaar, P. W. Laird, Genome-scale analysis of aberrant DNA methylation in colorectal cancer. *Genome Res.* **22**, 271–282 (2012).
14. H. J. Jang, G. Hostetter, A. W. MacFarlane, Z. Madaj, E. A. Ross, T. Hinoue, J. R. Kulchycki, R. S. Burgos, M. Tafseer, R. K. Alpaugh, C. L. Schwebel, R. Kokate, D. M. Geynisman, M. R. Zibelman, P. Ghatalia, P. W. Nichols, W. Chung, J. Madzo, N. M. Hahn, D. I. Quinn, J.-P. J. Issa, M. J. Topper, S. B. Baylin, H. Shen, K. S. Campbell, P. A. Jones, E. R. Plimack, A phase II trial of guadecitabine plus atezolizumab in metastatic urothelial carcinoma progressing after initial immune checkpoint inhibitor therapy. *Clin Cancer Res* **29**, 2052–2065 (2023).
15. C. Hu, X. Liu, Y. Zeng, J. Liu, F. Wu, DNA methyltransferase inhibitors combination therapy for the treatment of solid tumor: Mechanism and clinical application. *Clin. Epigenetics* **13**, 166 (2021).
16. S. Feng, D. D. De Carvalho, Clinical advances in targeting epigenetics for cancer therapy. *FEBS J.* **289**, 1214–1239 (2022).
17. N. Azad, C. A. Zahnow, C. M. Rudin, S. B. Baylin, The future of epigenetic therapy in solid tumours—Lessons from the past. *Nat. Rev. Clin. Oncol.* **10**, 256–266 (2013).
18. T. Sato, J.-P. J. Issa, P. Kropf, DNA hypomethylating drugs in cancer therapy. *Cold Spring Harb. Perspect. Med.* **7**, a026948 (2017).
19. H. Fan, X. Lu, X. Wang, Y. Liu, B. Guo, Y. Zhang, W. Zhang, J. Nie, K. Feng, M. Chen, Y. Zhang, Y. Wang, F. Shi, X. Fu, H. Zhu, W. Han, Low-dose decitabine-based chemoimmunotherapy for patients with refractory advanced solid tumors: A phase I/II report. *J. Immunol. Res.* **2014**, 371087 (2014).
20. P. Fenaux, G. J. Mufti, E. Hellstrom-Lindberg, V. Santini, C. Finelli, A. Giagounidis, R. Schoch, N. Gattermann, G. Sanz, A. List, S. D. Gore, J. F. Seymour, J. M. Bennett, J. Byrd, J. Backstrom, L. Zimmerman, D. McKenzie, C. L. Beach, L. R. Silverman, Efficacy of azacitidine compared with that of conventional care regimens in the treatment of higher-risk myelodysplastic syndromes: A randomised, open-label, phase III study. *Lancet Oncol.* **10**, 223–232 (2009).
21. M. Karahoca, R. L. Momparler, Pharmacokinetic and pharmacodynamic analysis of 5-aza-2′-deoxycytidine (decitabine) in the design of its dose-schedule for cancer therapy. *Clin. Epigenetics* **5**, 3 (2013).
22. A. Sharma, R. Vatapalli, E. Abdelfatah, K. W. McMahon, Z. Kerner, A. A. Guzzetta, J. Singh, C. Zahnow, S. B. Baylin, S. Yerram, Y. Hu, N. Azad, N. Ahuja, Hypomethylating agents synergize with irinotecan to improve response to chemotherapy in colorectal cancer cells. *PLOS ONE* **12**, e0176139 (2017).
23. H.-C. Tsai, H. Li, L. Van Neste, Y. Cai, C. Robert, F. V. Rassool, J. J. Shin, K. M. Harbom, R. Beaty, E. Pappou, J. Harris, R.-W. C. Yen, N. Ahuja, M. V. Brock, V. Stearns, D. Feller-Kopman, L. B. Yarmus, Y.-C. Lin, A. L. Welm, J.-P. Issa, I. Minn, W. Matsui, Y.-Y. Jang, S. J. Sharkis, S. B. Baylin, C. A. Zahnow, Transient low doses of DNA-demethylating agents exert durable antitumor effects on hematological and epithelial tumor cells. *Cancer Cell* **21**, 430–446 (2012).

24. P. A. Jones, H. Ohtani, A. Chakravarthy, D. D. De Carvalho, Epigenetic therapy in immune-oncology. *Nat. Rev. Cancer* **19**, 151–161 (2019).
25. A. Laugesen, J. W. Højfeldt, K. Helin, Molecular mechanisms directing PRC2 recruitment and H3K27 methylation. *Mol. Cell* **74**, 8–18 (2019).
26. B. E. Bernstein, T. S. Mikkelsen, X. Xie, M. Kamal, D. J. Huebert, J. Cuff, B. Fry, A. Meissner, M. Wernig, K. Plath, R. Jaenisch, A. Wagschal, R. Feil, S. L. Schreiber, E. S. Lander, A bivalent chromatin structure marks key developmental genes in embryonic stem cells. *Cell* **125**, 315–326 (2006).
27. L. Di Croce, K. Helin, Transcriptional regulation by Polycomb group proteins. *Nat. Struct. Mol. Biol.* **20**, 1147–1155 (2013).
28. H. Easwaran, S. E. Johnstone, L. Van Neste, J. Ohm, T. Mosbruger, Q. Wang, M. J. Aryee, P. Joyce, N. Ahuja, D. Weisenberger, E. Collisson, J. Zhu, S. Yegnasubramanian, W. Matsui, S. B. Baylin, A DNA hypermethylation module for the stem/progenitor cell signature of cancer. *Genome Res.* **22**, 837–849 (2012).
29. E. N. Gal-Yam, G. Egger, L. Iniguez, H. Holster, S. Einarsson, X. Zhang, J. C. Lin, G. Liang, P. A. Jones, A. Tanay, Frequent switching of Polycomb repressive marks and DNA hypermethylation in the PC3 prostate cancer cell line. *Proc. Natl. Acad. Sci. U.S.A.* **105**, 12979–12984 (2008).
30. F. D. Lay, Y. Liu, T. K. Kelly, H. Witt, P. J. Farnham, P. A. Jones, B. P. Berman, The role of DNA methylation in directing the functional organization of the cancer epigenome. *Genome Res.* **25**, 467–477 (2015).
31. G. Liang, D. J. Weisenberger, DNA methylation aberrancies as a guide for surveillance and treatment of human cancers. *Epigenetics* **12**, 416–432 (2017).
32. V. K. Tiwari, K. M. McGarvey, J. D. F. Licchesi, J. E. Ohm, J. G. Herman, D. Schübeler, S. B. Baylin, PcG proteins, DNA methylation, and gene repression by chromatin looping. *PLOS Biol.* **6**, 2911–2927 (2008).
33. K. M. McGarvey, L. Van Neste, L. Cope, J. E. Ohm, J. G. Herman, W. Van Criekinge, K. E. Schuebel, S. B. Baylin, Defining a chromatin pattern that characterizes DNA-hypermethylated genes in colon cancer cells. *Cancer Res.* **68**, 5753–5759 (2008).
34. G. Deblois, S. A. M. Tonekaboni, G. Grillo, C. Martinez, Y. I. Kao, F. Tai, I. Ettayebi, A.-M. Fortier, P. Savage, A. N. Fedor, X. Liu, P. Guilhamon, E. Lima-Fernandes, A. Murison, H. Kuasne, W. Ba-alawi, D. W. Cescon, C. H. Arrowsmith, D. D. D. Carvalho, B. Haibe-Kains, J. W. Locasale, M. Park, M. Lupien, Epigenetic switch-induced viral mimicry evasion in chemotherapy resistant breast cancer. *Cancer Discov.* **10**, 1312–1329 (2020).
35. K. Dimopoulos, A. S. Helbo, H. F. Munch-Petersen, L. Sjö, J. Christensen, L. S. Kristensen, F. Asmar, N. E. U. Hermansen, C. O'Connel, P. Gimsing, G. Liang, K. Grønbæk, Dual inhibition of DNMTs and EZH2 can overcome both intrinsic and acquired resistance of myeloma cells to IMiDs in a cereblon-independent manner. *Mol. Oncol.* **12**, 180–195 (2018).
36. Y. Li, E. M. Goldberg, X. Chen, X. Xu, J. T. McGuire, G. Leuzzi, D. Karagiannis, T. Tate, N. Farhangdoost, C. Horth, E. Dai, Z. Li, Z. Zhang, B. Izar, J. Que, A. Ciccia, J. Majewski, A. J. Yoon, L. Ailles, C. L. Mendelsohn, C. Lu, Histone methylation antagonism drives tumor immune evasion in squamous cell carcinomas. *Mol. Cell* **82**, 3901–3918.e7 (2022).
37. Y. Kurahashi, T. Watanabe, Y. Yamamoto, H. Ureshino, K. Kamachi, N. Yoshida-Sakai, Y. Fukuda-Kurahashi, S. Yamashita, N. Hattori, H. Nakamura, A. Kawaguchi, T. Ushijima, E. Sueoka, S. Kimura, Dual targeting of aberrant DNA and histone methylation synergistically suppresses tumor cell growth in *ATL*. *Blood Adv.* **7**, 1545–1559 (2023).
38. R. L. Momparler, S. Côté, L. F. Momparler, Y. Idaghdour, Inhibition of DNA and histone methylation by 5-aza-2′-deoxycytidine (decitabine) and 3-deazaneplanocin-A on antineoplastic action and gene expression in myeloid leukemic cells. *Front. Oncol.* **7**, 19 (2017).
39. H. Takeshima, M. Wakabayashi, N. Hattori, S. Yamashita, T. Ushijima, Identification of coexistence of DNA methylation and H3K27me3 specifically in cancer cells as a promising target for epigenetic therapy. *Carcinogenesis* **36**, 192–201 (2015).
40. L. Zhang, H.-T. Li, R. Shereda, Q. Lu, D. J. Weisenberger, C. O'Connell, K. Machida, W. An, H.-J. Lenz, A. El-Khoueiry, P. A. Jones, M. Liu, G. Liang, DNMT and EZH2 inhibitors synergize to activate therapeutic targets in hepatocellular carcinoma. *Cancer Lett.* **548**, 215899 (2022).
41. M.-L. Eich, M. Athar, J. E. Ferguson III, S. Varambally, EZH2-targeted therapies in cancer: Hype or a reality. *Cancer Res.* **80**, 5449–5458 (2020).
42. F. Morschhauser, H. Tilly, A. Chaidos, P. McKay, T. Phillips, S. Assouline, C. L. Batlevi, P. Campbell, V. Ribrag, G. L. Damaj, M. Dickinson, W. Jurczak, M. Kazmierczak, S. Opat, J. Radford, A. Schmitt, J. Yang, J. Whalen, S. Agarwal, D. Adib, G. Salles, Tazemetostat for patients with relapsed or refractory follicular lymphoma: An open-label, single-arm, multicentre, phase 2 trial. *Lancet Oncol.* **21**, 1433–1442 (2020).
43. S. B. Rothbart, S. B. Baylin, Epigenetic therapy for epithelioid sarcoma. *Cell* **181**, 211 (2020).
44. Y. Cui, F. Hausheer, R. Beaty, C. Zahnow, J. P. Issa, F. Bunz, S. B. Baylin, A recombinant reporter system for monitoring reactivation of an endogenously DNA hypermethylated gene. *Cancer Res.* **74**, 3834–3843 (2014).
45. G. Egger, S. Jeong, S. G. Escobar, C. C. Cortez, T. W. H. Li, Y. Saito, C. B. Yoo, P. A. Jones, G. Liang, Identification of DNMT1 (DNA methyltransferase 1) hypomorphs in somatic knockouts suggests an essential role for DNMT1 in cell survival. *Proc. Natl. Acad. Sci. U.S.A.* **103**, 14080–14085 (2006).
46. H. S. Rugo, I. Jacobs, S. Sharma, F. Scappaticci, T. A. Paul, K. Jensen-Pergakes, G. G. Malouf, The promise for histone methyltransferase inhibitors for epigenetic therapy in clinical oncology: A narrative review. *Adv. Ther.* **37**, 3059–3082 (2020).
47. S. Wang, S. C. Ordonez-Rubiano, A. Dhiman, G. Jiao, B. P. Strohmier, C. J. Krusemark, E. C. Dykhuizen, Polycomb group proteins in cancer: Multifaceted functions and strategies for modulation. *Cancer* **3**, zcab039 (2021).
48. Y. Liu, Q. Yang, The roles of EZH2 in cancer and its inhibitors. *Med. Oncol.* **40**, 167 (2023).
49. S. S. Palii, B. O. Van Emburgh, U. T. Sankpal, K. D. Brown, K. D. Robertson, DNA methylation inhibitor 5-aza-2′-deoxycytidine induces reversible genome-wide DNA Damage that is distinctly influenced by DNA methyltransferases 1 and 3B. *Mol. Cell. Biol.* **28**, 752–771 (2008).
50. M. B. Pappalardi, K. Keenan, M. Cockerill, W. A. Kellner, A. Stowell, C. Sherk, K. Wong, S. Pathuri, J. Briand, M. Steidel, P. Chapman, A. Groy, A. K. Wiseman, C. F. McHugh, N. Campobasso, A. P. Graves, E. Fairweather, T. Werner, A. Raoof, R. J. Butlin, L. Rueda, J. R. Horton, D. T. Fosbenner, C. Zhang, J. L. Handler, M. Muliaditan, M. Mebrahtu, J.-P. Jaworski, D. E. McNulty, C. Burt, H. C. Eberl, A. N. Taylor, T. Ho, S. Merrihew, S. W. Foley, A. Rutkowska, M. Li, S. P. Romeril, K. Goldberg, X. Zhang, C. S. Kershaw, M. Bantscheff, A. J. Jurewicz, E. Minthorn, P. Grandi, M. Patel, A. B. Benowitz, H. P. Mohammad, A. G. Gilmartin, R. K. Prinjha, D. Ogilvie, C. Carpenter, D. Heerding, S. B. Baylin, P. A. Jones, X. Cheng, B. W. King, J. I. Luengo, A. M. Jordan, I. Waddell, R. G. Kruger, M. T. McCabe, Discovery of a first-in-class reversible DNMT1-selective inhibitor with improved tolerability and efficacy in acute myeloid leukemia. *Nat. Cancer* **2**, 1002–1017 (2021).
51. A. Ianevski, A. K. Giri, T. Aittokallio, SynergyFinder 2.0: Visual analytics of multi-drug combination synergies: Visual analytics of multi-drug combination synergies. *Nucleic Acids Res.* **48**, W488–W493 (2020).
52. K. C. G. Berg, P. W. Eide, I. A. Eilertsen, B. Johannessen, J. Bruun, S. A. Danielsen, M. Bjørnslett, L. A. Meza-Zepeda, M. Eknæs, G. E. Lind, O. Myklebost, R. I. Skotheim, A. Sveen, R. A. Lothe, Multi-omics of 34 colorectal cancer cell lines - a resource for biomedical studies. *Mol. Cancer* **16**, 116 (2017).
53. S. Kawano, A. R. Grassian, M. Tsuda, S. K. Knutson, N. M. Warholic, G. Kuznetsov, S. Xu, Y. Xiao, R. M. Pollock, J. S. Smith, K. K. Kuntz, S. Ribich, Y. Minoshima, J. Matsui, R. A. Copeland, S. Tanaka, H. Keilhack, Preclinical evidence of anti-tumor activity induced by EZH2 inhibition in human models of synovial sarcoma. *PLOS ONE* **11**, e0158888 (2016).
54. S. K. Knutson, N. M. Warholic, T. J. Wigle, C. R. Klaus, C. J. Allain, A. Raimondi, M. Porter Scott, R. Chesworth, M. P. Moyer, R. A. Copeland, V. M. Richon, R. M. Pollock, K. W. Kuntz, H. Keilhack, Durable tumor regression in genetically altered malignant rhabdoid tumors by inhibition of methyltransferase EZH2. *Proc. Natl. Acad. Sci. U.S.A.* **110**, 7922–7927 (2013).
55. S. K. Knutson, T. J. Wigle, N. M. Warholic, C. J. Sneeringer, C. J. Allain, C. R. Klaus, J. D. Sacks, A. Raimondi, C. R. Majer, J. Song, M. P. Scott, L. Jin, J. J. Smith, E. J. Olhava, R. Chesworth, M. P. Moyer, V. M. Richon, R. A. Copeland, H. Keilhack, R. M. Pollock, K. W. Kuntz, A selective inhibitor of EZH2 blocks H3K27 methylation and kills mutant lymphoma cells. *Nat. Chem. Biol.* **8**, 890–896 (2012).
56. T. Qin, R. Castoro, S. El Ahdab, J. Jelinek, X. Wang, J. Si, J. Shu, R. He, N. Zhang, W. Chung, H. M. Kantarjian, J.-P. J. Issa, Mechanisms of resistance to decitabine in the myelodysplastic syndrome. *PLOS ONE* **6**, e23372 (2011).
57. H. Kantarjian, Y. Oki, G. Garcia-Manero, X. Huang, S. O'Brien, J. Cortes, S. Faderl, C. Bueso-Ramos, F. Ravandi, Z. Estrov, A. Ferrajoli, W. Wierda, J. Shan, J. Davis, F. Giles, H. I. Saba, J.-P. J. Issa, Results of a randomized study of 3 schedules of low-dose decitabine in higher-risk myelodysplastic syndrome and chronic myelomonocytic leukemia. *Blood* **109**, 52–57 (2007).
58. G. Jacquemin, A. Wurmser, M. Huyghe, W. Sun, Z. Homayed, C. Merle, M. Perkins, F. Qasrawi, S. Richon, F. Dingli, G. Arras, D. Loew, D. Vignjevic, J. Pannequin, S. Fre, Paracrine signalling between intestinal epithelial and tumour cells induces a regenerative programme. *eLife* **11**, e76541 (2022).
59. B. M. Dickson, A. Kupai, R. M. Vaughan, S. B. Rothbart, Streamlined quantitative analysis of histone modification abundance at nucleosome-scale resolution with siQ-ChIP version 2.0. *Sci. Rep.* **13**, 7508 (2023).
60. B. M. Dickson, R. L. Tiedemann, A. A. Chomiak, E. M. Cornett, R. M. Vaughan, S. B. Rothbart, A physical basis for quantitative ChIP-sequencing. *J. Biol. Chem.* **295**, 15826–15837 (2020).
61. B. Bonev, G. Cavalli, Organization and function of the 3D genome. *Nat. Rev. Genet.* **17**, 661–678 (2016).
62. S. E. Johnstone, A. Reyes, Y. Qi, C. Adriaens, E. Hegazi, K. Pelka, J. H. Chen, L. S. Zou, Y. Drier, V. Hecht, N. Shoresh, M. K. Selig, C. A. Lareau, S. Iyer, S. C. Nguyen, E. F. Joyce, N. Hacohen, R. A. Irizarry, B. Zhang, M. J. Aryee, B. E. Bernstein, Large-scale topological changes restrain malignant progression in colorectal cancer. *Cell* **182**, 1474–1489.e23 (2020).
63. P. A. Zhao, T. Sasaki, D. M. Gilbert, High-resolution Repli-Seq defines the temporal choreography of initiation, elongation and termination of replication in mammalian cells. *Genome Biol.* **21**, 76 (2020).
64. J. Dekker, A. S. Belmont, M. Guttman, V. O. Leshyk, J. T. Lis, S. Lomvardas, L. A. Mirny, C. C. O'Shea, P. J. Park, B. Ren, J. C. R. Politz, J. Shendure, S. Zhong, The 4D nucleome project. *Nature* **549**, 219–226 (2017).

65. J. E. Ohm, K. M. McGarvey, X. Yu, L. Cheng, K. E. Schuebel, L. Cope, H. P. Mohammad, W. Chen, V. C. Daniel, W. Yu, D. M. Berman, T. Jenuwein, K. Pruitt, S. J. Sharkis, D. N. Watkins, J. G. Herman, S. B. Baylin, A stem cell-like chromatin pattern may predispose tumor suppressor genes to DNA hypermethylation and heritable silencing. *Nat. Genet.* **39**, 237–242 (2007).
66. M. Widschwendter, H. Fiegl, D. Egle, E. Mueller-Holzner, G. Spizzo, C. Marth, D. J. Weisenberger, M. Campan, J. Young, I. Jacobs, P. W. Laird, Epigenetic stem cell signature in cancer. *Nat. Genet.* **39**, 157–158 (2007).
67. A. B. Brinkman, H. Gu, S. J. J. Bartels, Y. Zhang, F. Matarese, F. Simmer, H. Marks, C. Bock, A. Gnirke, A. Meissner, H. G. Stunnenberg, Sequential ChIP-bisulfite sequencing enables direct genome-scale investigation of chromatin and DNA methylation cross-talk. *Genome Res.* **22**, 1128–1138 (2012).
68. A. L. Statham, M. D. Robinson, J. Z. Song, M. W. Coolen, C. Stirzaker, S. J. Clark, Bisulfite sequencing of chromatin immunoprecipitated DNA (BisChIP-seq) directly informs methylation status of histone-modified DNA. *Genome Res.* **22**, 1120–1127 (2012).
69. M. Arai, O. Yokosuka, Y. Hirasawa, K. Fukai, T. Chiba, F. Imazeki, T. Kanda, M. Yatomi, Y. Takiguchi, N. Seki, H. Saisho, T. Ochiai, Sequential gene expression changes in cancer cell lines after treatment with the demethylation agent 5-aza-2′-deoxycytidine. *Cancer* **106**, 2514–2525 (2006).
70. M. J. Topper, M. Vaz, K. B. Chiappinelli, C. E. DeStefano Shields, N. Niknafs, R.-W. C. Yen, A. Wenzel, J. Hicks, M. Ballew, M. Stone, P. T. Tran, C. A. Zahnow, M. D. Hellmann, V. Anagnostou, P. L. Strissel, R. Strick, V. E. Velculescu, S. B. Baylin, Epigenetic therapy ties MYC depletion to reversing immune evasion and treating lung cancer. *Cell* **171**, 1284–1300.e21 (2017).
71. X. Yang, H. Han, D. D. De Carvalho, F. D. Lay, P. A. Jones, G. Liang, Gene body methylation can alter gene expression and is a therapeutic target in cancer. *Cancer Cell* **26**, 577–590 (2014).
72. N. J.-M. Raynal, J. T. Lee, Y. Wang, A. Beaudry, P. Madireddi, J. Garriga, G. Malouf, S. Dumont, E. J. Dettman, V. Gharibyan, S. Ahmed, W. Chung, W. E. Childers, M. Abou-Gharbia, R. A. Henry, A. J. Andrews, J. Jelinek, Y. Cui, S. B. Baylin, D. L. Gill, J.-P. J. Issa, Targeting calcium signaling induces epigenetic reactivation of tumor suppressor genes in cancer. *Cancer Res.* **76**, 1494–1505 (2016).
73. Y.-J. Park, S.-A. Yoo, M. Kim, W.-U. Kim, The role of calcium–calcineurin–NFAT signaling pathway in health and autoimmune diseases. *Front. Immunol.* **11**, (2020).
74. M. B. F. Werneck, E. Hottz, P. T. Bozza, J. P. B. Viola, Cyclosporin A inhibits colon cancer cell growth independently of the calcineurin pathway. *Cell Cycle* **11**, 3997–4008 (2012).
75. M. Mahmudpour, J. Roozbeh, M. Keshavarz, S. Farrokhi, I. Nabipour, COVID-19 cytokine storm: The anger of inflammation. *Cytokine* **133**, 155151 (2020).
76. H. Li, K. B. Chiappinelli, A. A. Guzzetta, H. Easwaran, R.-W. C. Yen, R. Vatapalli, M. J. Topper, J. Luo, R. M. Connolly, N. S. Azad, V. Stearns, D. M. Pardoll, N. Davidson, P. A. Jones, D. J. Slamon, S. B. Baylin, C. A. Zahnow, N. Ahuja, Immune regulation by low doses of the DNA methyltransferase inhibitor 5-azacitidine in common human epithelial cancers. *Oncotarget* **5**, 587–598 (2014).
77. The Cancer Genome Atlas Network, Comprehensive molecular portraits of human breast tumours. *Nature* **490**, 61–70 (2012).
78. Cancer Genome Atlas Research Network, Integrated genomic analyses of ovarian carcinoma. *Nature* **474**, 609–615 (2011).
79. T. Sato, M. Cesaroni, W. Chung, S. Panjarian, A. Tran, J. Madzo, Y. Okamoto, H. Zhang, X. Chen, J. Jelinek, J.-P. J. Issa, Transcriptional selectivity of epigenetic therapy in cancer. *Cancer Res.* **77**, 470–481 (2017).
80. M.-Y. Chen, W. S.-L. Liao, Z. Lu, W. G. Bornmann, V. Hennessey, M. N. Washington, G. L. Rosner, Y. Yu, A. A. Ahmed, R. C. Bast, Decitabine and suberoylanilide hydroxamic acid (SAHA) inhibit growth of ovarian cancer cell lines and xenografts while inducing expression of imprinted tumor suppressor genes, apoptosis, G2/M arrest, and autophagy. *Cancer* **117**, 4424–4438 (2011).
81. H. Yang, K. Hoshino, B. Sanchez-Gonzalez, H. Kantarjian, G. Garcia-Manero, Antileukemia activity of the combination of 5-aza-2′-deoxycytidine with valproic acid. *Leuk. Res.* **29**, 739–748 (2005).
82. J. P. Bewersdorf, R. Shallis, M. Stahl, A. M. Zeidan, Epigenetic therapy combinations in acute myeloid leukemia: What are the options? *Adv. Ther.* **10**, 204062071881669 (2019).
83. R. M. Connolly, H. Li, R. C. Jankowitz, Z. Zhang, M. A. Rudek, S. C. Jeter, S. A. Slater, P. Powers, A. C. Wolff, J. H. Fetting, A. Brufsky, R. Piekarz, N. Ahuja, P. W. Laird, H. Shen, D. J. Weisenberger, L. Cope, J. G. Herman, G. Somlo, A. A. Garcia, P. A. Jones, S. B. Baylin, N. E. Davidson, C. A. Zahnow, V. Stearns, Combination epigenetic therapy in advanced breast cancer with 5-azacitidine and entinostat: A phase II National Cancer Institute/stand up to cancer study. *Clin. Cancer Res.* **23**, 2691–2701 (2017).
84. J. How, M. D. Minden, L. Brian, E. X. Chen, J. Brandwein, A. C. Schuh, A. D. Schimmer, V. Gupta, S. Webster, T. Degelder, P. Haines, L.-A. Stayner, S. McGill, L. Wang, R. Piekarz, T. Wong, L. L. Siu, I. Espinoza-Delgado, J. L. Holleran, M. J. Egorin, K. W. L. Yee, A phase I trial of two sequence-specific schedules of decitabine and vorinostat in patients with acute myeloid leukemia. *Leuk. Lymphoma* **56**, 2793–2802 (2015).
85. M. A. Sekeres, M. Othus, A. F. List, O. Odenike, R. M. Stone, S. D. Gore, M. R. Litzow, R. Buckstein, M. Fang, D. Roulston, C. D. Bloomfield, A. Moseley, A. Nazha, Y. Zhang, M. R. Velasco, R. Gaur, E. Atallah, E. C. Attar, E. K. Cook, A. H. Cull, M. J. Rauh, F. R. Appelbaum, H. P. Erba, Randomized phase II study of azacitidine alone or in combination with lenalidomide or with vorinostat in higher-risk myelodysplastic syndromes and chronic myelomonocytic leukemia: North american intergroup study SWOG S1117. *J. Clin. Oncol.* **35**, 2745–2753 (2017).
86. B. Ball, A. Zeidan, S. D. Gore, T. Prebet, Hypomethylating agent combination strategies in myelodysplastic syndromes: Hopes and shortcomings. *Leuk. Lymphoma* **58**, 1022–1036 (2017).
87. T. E. Fandy, J. G. Herman, P. Kerns, A. Jiemjit, E. A. Sugar, S.-H. Choi, A. S. Yang, T. Aucott, T. Dauses, R. Odchimar-Reissig, J. Licht, M. J. McConnell, C. Nasrallah, M. K. H. Kim, W. Zhang, Y. Sun, A. Murgo, I. Espinoza-Delgado, K. Oteiza, I. Owoeye, L. R. Silverman, S. D. Gore, H. E. Carraway, Early epigenetic changes and DNA damage do not predict clinical response in an overlapping schedule of 5-azacytidine and entinostat in patients with myeloid malignancies. *Blood* **114**, 2764–2773 (2009).
88. S. K. Kachhap, N. Rosmus, S. J. Collis, M. S. Q. Kortenhorst, M. D. Wissing, M. Hedayati, S. Shabbeer, J. Mendonca, J. Deangelis, L. Marchionni, J. Lin, N. Höti, J. W. R. Nortier, T. L. DeWeese, H. Hammers, M. A. Carducci, Downregulation of homologous recombination DNA repair genes by HDAC inhibition in prostate cancer is mediated through the E2F1 transcription factor. *PLOS ONE* **5**, e11208 (2010).
89. C. Robert, F. V. Rassool, HDAC inhibitors. *Adv. Cancer Res.* **116**, 87–129 (2012).
90. Y. Liu, T. Liang, X. Qiu, X. Ye, Z. Li, B. Tian, D. Yan, Down-regulation of Nfatc1 suppresses proliferation, migration, invasion, and warburg effect in prostate cancer cells. *Med. Sci. Monit.* **25**, 1572–1581 (2019).
91. M. R. Müller, A. Rao, NFAT, immunity and cancer: A transcription factor comes of age. *Nat. Rev. Immunol.* **10**, 645–656 (2010).
92. M. Vaeth, S. Feske, NFAT control of immune function: New frontiers for an abiding trooper. *F1000Res* **7**, 260 (2018).
93. S. Goswami, I. Apostolou, J. Zhang, J. Skepner, S. Anandhan, X. Zhang, L. Xiong, P. Trojer, A. Aparicio, S. K. Subudhi, J. P. Allison, H. Zhao, P. Sharma, Modulation of EZH2 expression in T cells improves efficacy of anti-CTLA-4 therapy. *J. Clin. Invest.* **128**, 3813–3818 (2018).
94. X. Li, Y. Zhang, M. Chen, Q. Mei, Y. Liu, K. Feng, H. Jia, L. Dong, L. Shi, L. Liu, J. Nie, W. Han, Increased IFNγ^+ T cells are responsible for the clinical responses of low-dose DNA-demethylating agent decitabine antitumor therapy. *Clin. Cancer Res.* **23**, 6031–6043 (2017).
95. H. Loo Yau, E. Bell, I. Ettayebi, F. C. de Almeida, G. M. Boukhaled, S. Y. Shen, D. Allard, B. Morancho, S. A. Marhon, C. A. Ishak, I. M. Gonzaga, T. da Silva Medina, R. Singhania, A. Chakravarthy, R. Chen, P. Mehdipour, S. Pommey, C. Klein, G. P. Amarante-Mendes, D. Roulois, J. Arribas, J. Stagg, D. G. Brooks, D. D. De Carvalho, DNA hypomethylating agents increase activation and cytolytic activity of CD8$^+$ T cells. *Mol. Cell* **81**, 1469–1483.e8 (2021).
96. D. Wang, J. Quiros, K. Mahuron, C.-C. Pai, V. Ranzani, A. Young, S. Silveria, T. Harwin, A. Abnousian, M. Pagani, M. D. Rosenblum, F. Van Gool, L. Fong, J. A. Bluestone, M. DuPage, Targeting EZH2 reprograms intratumoral regulatory T cells to enhance cancer immunity. *Cell Rep.* **23**, 3262–3274 (2018).
97. I. H. Sahin, K. K. Ciombor, L. A. Diaz, J. Yu, R. Kim, Immunotherapy for microsatellite stable colorectal cancers: Challenges and novel therapeutic avenues. *Am. Soc. Clin. Oncol. Educ. Book* **42**, 242–253 (2022).
98. S. H. Barghout, M. K. Mann, A. Aman, Y. Yu, M. G. Alteen, A. D. Schimmer, M. Schapira, C. H. Arrowsmith, D. Barsyte-Lovejoy, Combinatorial anticancer drug screen identifies off-target effects of epigenetic chemical probes. *ACS Chem. Biol.* **17**, 2801–2816 (2022).
99. A. Lin, C. J. Giuliano, A. Palladino, K. M. John, C. Abramowicz, M. L. Yuan, E. L. Sausville, D. A. Lukow, L. Liu, A. R. Chait, Z. C. Galluzzo, C. Tucker, J. M. Sheltzer, Off-target toxicity is a common mechanism of action of cancer drugs undergoing clinical trials. *Sci. Transl. Med.* **11**, eaaw8412 (2019).
100. M. A. Hahn, T. Hahn, D.-H. Lee, R. S. Esworthy, B.-W. Kim, A. D. Riggs, F.-F. Chu, G. P. Pfeifer, Methylation of polycomb target genes in intestinal cancer is mediated by inflammation. *Cancer Res.* **68**, 10280–10289 (2008).
101. G. C. Hon, R. D. Hawkins, O. L. Caballero, C. Lo, R. Lister, M. Pelizzola, A. Valsesia, Z. Ye, S. Kuan, L. E. Edsall, A. A. Camargo, B. J. Stevenson, J. R. Ecker, V. Bafna, R. L. Strausberg, A. J. Simpson, B. Ren, Global DNA hypomethylation coupled to repressive chromatin domain formation and gene silencing in breast cancer. *Genome Res.* **22**, 246–258 (2012).
102. M. Walter, A. Teissandier, R. Pérez-Palacios, D. Bourc'his, An epigenetic switch ensures transposon repression upon dynamic loss of DNA methylation in embryonic stem cells. *eLife* **5**, e11418 (2016).
103. S. B. Rothbart, B. M. Dickson, J. R. Raab, A. T. Grzybowski, K. Krajewski, A. H. Guo, E. K. Shanle, S. Z. Josefowicz, S. M. Fuchs, C. D. Allis, T. R. Magnuson, A. J. Ruthenburg, B. D. Strahl, An interactive database for the assessment of histone antibody specificity. *Mol. Cell* **59**, 502–511 (2015).
104. K. J. Livak, T. D. Schmittgen, Analysis of relative gene expression data using real-time quantitative PCR and the 2(−delta delta C(T)) method. *Methods* **25**, 402–408 (2001).
105. G. G. Faust, I. M. Hall, SAMBLASTER: Fast duplicate marking and structural variant read extraction. *Bioinformatics* **30**, 2503–2505 (2014).
106. J. Ernst, M. Kellis, Chromatin-state discovery and genome annotation with ChromHMM. *Nat. Protoc.* **12**, 2478–2492 (2017).

107. A. R. Quinlan, I. M. Hall, BEDTools: A flexible suite of utilities for comparing genomic features. *Bioinformatics* **26**, 841–842 (2010).
108. F. Ramírez, F. Dündar, S. Diehl, B. A. Grüning, T. Manke, deepTools: A flexible platform for exploring deep-sequencing data. *Nucleic Acids Res.* **42**, W187–W191 (2014).
109. S. Heinz, C. Benner, N. Spann, E. Bertolino, Y. C. Lin, P. Laslo, J. X. Cheng, C. Murre, H. Singh, C. K. Glass, Simple combinations of lineage-determining transcription factors prime cis-regulatory elements required for macrophage and B cell identities. *Mol. Cell* **38**, 576–589 (2010).
110. M. Bibikova, J. Le, B. Barnes, S. Saedinia-Melnyk, L. Zhou, R. Shen, K. L. Gunderson, Genome-wide DNA methylation profiling using Infinium® assay. *Epigenomics* **1**, 177–200 (2009).
111. M. Bibikova, B. Barnes, C. Tsan, V. Ho, B. Klotzle, J. M. Le, D. Delano, L. Zhang, G. P. Schroth, K. L. Gunderson, J.-B. Fan, R. Shen, High density DNA methylation array with single CpG site resolution. *Genomics* **98**, 288–295 (2011).
112. W. Zhou, T. J. Triche, P. W. Laird, H. Shen, SeSAMe: Reducing artifactual detection of DNA methylation by Infinium BeadChips in genomic deletions. *Nucleic Acids Res.* **46**, e123 (2018).
113. W. Huber, V. J. Carey, R. Gentleman, S. Anders, M. Carlson, B. S. Carvalho, H. C. Bravo, S. Davis, L. Gatto, T. Girke, R. Gottardo, F. Hahne, K. D. Hansen, R. A. Irizarry, M. Lawrence, M. I. Love, J. MacDonald, V. Obenchain, A. K. Oleś, H. Pagès, A. Reyes, P. Shannon, G. K. Smyth, D. Tenenbaum, L. Waldron, M. Morgan, Orchestrating high-throughput genomic analysis with Bioconductor. *Nat. Methods* **12**, 115–121 (2015).
114. R. C. Gentleman, V. J. Carey, D. M. Bates, B. Bolstad, M. Dettling, S. Dudoit, B. Ellis, L. Gautier, Y. Ge, J. Gentry, K. Hornik, T. Hothorn, W. Huber, S. Iacus, R. Irizarry, F. Leisch, C. Li, M. Maechler, A. J. Rossini, G. Sawitzki, C. Smith, G. Smyth, L. Tierney, J. Y. H. Yang, J. Zhang, Bioconductor: Open software development for computational biology and bioinformatics. *Genome Biol.* **5**, R80 (2004).
115. T. Hulsen, J. de Vlieg, W. Alkema, BioVenn - A web application for the comparison and visualization of biological lists using area-proportional Venn diagrams. *BMC Genomics* **9**, 488 (2008).
116. W. R. Yang, D. Ardeljan, C. N. Pacyna, L. M. Payer, K. H. Burns, SQuIRE reveals locus-specific regulation of interspersed repeat expression. *Nucleic Acids Res.* **47**, e27 (2019).
117. A. Subramanian, P. Tamayo, V. K. Mootha, S. Mukherjee, B. L. Ebert, M. A. Gillette, A. Paulovich, S. L. Pomeroy, T. R. Golub, E. S. Lander, J. P. Mesirov, Gene set enrichment analysis: A knowledge-based approach for interpreting genome-wide expression profiles. *Proc. Natl. Acad. Sci. U.S.A.* **102**, 15545–15550 (2005).
118. A. Colaprico, T. C. Silva, C. Olsen, L. Garofano, C. Cava, D. Garolini, T. S. Sabedot, T. M. Malta, S. M. Pagnotta, I. Castiglioni, M. Ceccarelli, G. Bontempi, H. Noushmehr, TCGAbiolinks: An R/Bioconductor package for integrative analysis of TCGA data. *Nucleic Acids Res.* **44**, e71 (2016).
119. C. G. A. Network, Comprehensive molecular characterization of human colon and rectal cancer. *Nature* **487**, 330–337 (2012).
120. ENCODE Project Consortium, An integrated encyclopedia of DNA elements in the human genome. *Nature* **489**, 57–74 (2012).

Acknowledgments: We thank members of the Rothbart and Baylin laboratories, P. Laird, and members of the Epigenetic Therapies SPORE for discussions. We also thank K. Foy and N. Vander Schaaf for assisting with harvesting intestinal adenomas from Apc$^{Min/+}$ mice, B. Johnson and J. Jang for discussions on bioinformatic analyses, and D. Chandler for critical reading of the manuscript. We acknowledge support from the Van Andel Institute Genomics Core (RRID:SCR_022913), Bioinformatics and Biostatistics Core, Flow Cytometry Core (RRID:SCR_022685), and Optical Imaging Core (RRID:SCR_021968). **Funding:** This work was supported by: National Institutes of Health grants R35GM124736 (to S.B.R.), P50CA254897 (to S.B.R.), and P50CA254897 (to S.B.B.); National Institutes of Health fellowship F32CA225043 (to A.A.C.); The American Cancer Society RSG-21-031-01-DMC (to S.B.R.); and The American Cancer Society Michigan Cancer Research Fund PF-16-245-01-DMC (to R.L.T.). **Author contributions:** Conceptualization: A.A.C., R.L.T., and S.B.R. Methodology: A.A.C. and R.L.T. Software: R.L.T. Validation: A.A.C., R.L.T., Y.L., A.K.W., and K.E.T. Formal analysis: A.A.C. and R.L.T. Investigation: A.A.C., R.L.T., Y.L., X.K., Y.C., A.K.W., K.E.T., and E.M.C. Resources: S.B.B. Data curation: A.A.C. and R.L.T. Writing—original draft: A.A.C., R.L.T., and S.B.R. Writing—review and editing: A.A.C., R.L.T., Y.L., K.E.T., E.M.C., M.J.T., S.B.B., and S.B.R. Visualization: A.A.C., R.L.T., Y.L., and A.K.W. Supervision: S.B.B. and S.B.R. Project administration: S.B.B. and S.B.R. Funding acquisition: A.A.C., R.L.T., S.B.B., and S.B.R. **Competing interests:** The authors declare that they have no competing interests. **Data and materials availability:** All data needed to evaluate the conclusions in the paper are present in the paper and/or the Supplementary Materials. All sequencing (EM-seq, siQ-ChIP, and total RNA-seq) and microarray (EPIC array) data have been deposited to the GEO under accession GSE237665 or can be accessed through ENCODE (EZH2 ChIP-seq fold change bigwigs: ENCSR046HGP). Code for processing and analysis is available at: https://github.com/rleetied/TAZDAC_Chomiak_2023. Release v1.0.0: https://zenodo.org/doi/10.5281/zenodo.10378553.

Submitted 25 August 2023
Accepted 21 February 2024
Published 27 March 2024
10.1126/sciadv.adk4423